

RESEARCH

Open Access



Development of a circadian-related prognostic signature highlights RBM17 as a stemness regulator in liver cancer

Jingsong Yan^{1†}, Xiao Yang^{2†}, Jiabin Lu³, Shasha Wu¹, Yanchen Wang⁴, Yuyang Du¹, Jingyi Zheng⁴, Fenfen Wang¹, Han Gao¹, Hui Yang¹, Shaoyan Xi^{3*} and Yan Li^{1,4*}

Abstract

The liver exhibits extensive circadian regulation among organs. Epidemiological studies have substantiated that disruptions in circadian rhythm constitute a risk factor for the oncogenesis of liver cancer. Nonetheless, the molecular underpinnings of how circadian dysregulation influences liver cancer progression remain elusive. Our research aims to elucidate these mechanisms and develop a predictive model for prognosis and treatment responsiveness. Our multi-omics analysis revealed extensive dysregulation of liver circadian genes (LCGs) in liver cancer. Employing machine learning algorithms, we pinpointed four pivotal dysregulated LCGs. Through the integration of single-cell, bulk, and spatial transcriptomics, we further elucidated the interconnections between LCGs dysregulation and the tumor microenvironment. In vivo and in vitro experiments demonstrated that RBM17, identified as a crucial dysregulated LCG, promotes the progression of liver cancer and cisplatin resistance by facilitating cancer stem cell phenotype. The circadian prognosis scores (CPS), based on these four genes, effectively reflected the prognosis of liver cancer patients and their responses to various therapeutic interventions. Mechanism of Action (MOA) analysis suggested that high CPS level may sensitize tumors to cell cycle-targeted therapies. Collectively, our findings provide new insights into the interplay between liver circadian gene regulation and liver cancer progression, and propose novel therapeutic targets for liver cancer.

Keywords Biomarkers, RBM17, Liver cancer, Circadian genes

[†]Jingsong Yan and Xiao Yang equally contributed to the manuscript.

*Correspondence:

Shaoyan Xi

xishy@sysucc.org.cn

Yan Li

liyan181@smu.edu.cn

¹Department of Systems Biology, School of Life Sciences, Southern University of Science and Technology, Shenzhen 518055, China

²Institute of Life Sciences, Chongqing Medical University, Chongqing 400016, China

³Department of Pathology, State Key Laboratory of Oncology in South China, Collaborative Innovation Center for Cancer Medicine, Sun Yat-sen University Cancer Center, Guangzhou 510060, China

⁴Shenzhen Hospital, Southern Medical University, Shenzhen 518000, China

Introduction

Liver cancer remains a significant global health challenge, with an estimated incidence of over 1 million cases by 2025. The most common form of liver cancer is hepatocellular carcinoma (HCC) and it accounts for approximately 90% of cases [1]. Surgery is the primary treatment for liver cancer patients. However, for those with advanced or metastatic liver cancer, treatment options are very limited. The first-line therapy has predominantly included sorafenib and transarterial chemoembolization (TACE), which have yielded suboptimal median overall survival (OS) rates. Despite immune checkpoint inhibitors exhibiting considerable therapeutic



promise, the response rates are generally modest [2, 3]. Consequently, there is an urgent need to develop robust models predictive of the prognosis and therapy response in liver cancer. Additionally, exploring the underlying mechanisms will identify potential targets and provide a theoretical basis for drug development and clinical decision making.

Humans exhibit robust circadian rhythms that regulate a wide range of physiological processes. The circadian clock is an evolutionarily ancient and highly conserved timing mechanism that generates ~24-hour rhythms at multiple levels, from cells to organs to whole organisms, and synchronizes behaviors [4]. This intrinsic clock system enables living organisms to anticipate and respond to daily environmental changes by temporally coordinating gene expression profiles. Epidemiological studies suggest the potential involvement of the deregulated circadian clock in the pathophysiology of various malignancies. Of note, the liver is a highly metabolically active organ that is strongly influenced by feeding and fasting cycles, and circadian misalignment [4, 5]. Disrupted circadian rhythms are widely recognized to be involved in the pathological processes of various liver diseases, including nonalcoholic fatty liver disease (NAFLD), non-alcoholic steatohepatitis (NASH), and liver fibrosis, which can ultimately contribute to the development of liver cancer [6, 7].

Predictive models based on circadian genes are noteworthy due to their importance in liver cancer. However, most of such models were developed upon core clock genes [8–10]. A subset of core clock genes, such as CLOCK and BMAL1, among others, form the interlocked transcription-translational feedback loops that drive the rhythmic expression of circadian output genes. It's estimated that hundreds and even thousands of gene expression in mice is associated with the circadian rhythm [4, 5, 11]. Moreover, multiple levels of genetic, epigenetic, and transcriptional regulation contribute to the molecular clockwork. Therefore, current core clock biomarkers may not characterize tumor subtypes well due to the molecular heterogeneity of liver cancer. Integrating multi-omics analyses, including transcriptomic, genomics, and methylation sequencing data, with machine-learning algorithms can help predict the comprehensive association between circadian genes and liver cancer prognosis and therapy.

Despite their clear association, the exact mechanism underlying the tumorigenic effects of the circadian genes remains largely unknown. Circadian rhythm disorders may trigger or at least be involved in metabolic dysregulation, cell cycle control, angiogenesis, genomic instability, cancer stem cell (CSC) maintenance, immune evasion, drug sensitivity, etc [12–14]. However, many of these proposed mechanisms still lack experimental evidence and require further functional analyses and

validation. Moreover, the variation of the circadian clock among different cell types and its intricate interplay with the immune system and microenvironment niche makes the mechanism research more challenging. Bulk technologies could merely reflect the merged signals from heterogeneous cell groups. Therefore, single-cell analyses are essential to further dissect activities of circadian signaling pathways in a cell-type manner and predict their effects on immunotherapy response and immune features in liver cancer.

Here, we unveiled the extensive dysregulation of circadian genes and their intricate interactions with malignant pathways in liver cancer through a comprehensive multi-omics landscape analysis. We analyzed the dysregulation of pivotal circadian genes within the tumor microenvironment using single-cell datasets and machine learning algorithms. Additionally, our research explored the significant role of the key circadian prognostic gene, RBM17, in the regulation of CSCs, and confirmed its contributory effect on cisplatin resistance of liver cancer. We introduced novel circadian prognosis scores (CPS) that accurately reflect the prognosis and treatment response of liver cancer. Moreover, we proposed the potential therapeutic vulnerability of tumors with high circadian disruption to cell cycle-targeted drugs.

Materials and methods

Public data sources acquisition and preprocessing

The bulk RNA expression profiles containing the corresponding clinical survival information of liver cancer were collected from The Cancer Genome Atlas (TCGA, <https://www.cancer.gov/ccg/research/genome-sequencing/tcga>) and International Cancer Genome Consortium (ICGC, <https://dcc.icgc.org/>), including TCGA-LIHC (training set) and ICGC-LIRI-JP (validation set). Raw counts were converted to transcripts per kilobase million (TPM), and log₂ transformed (TPM + 1). The Sorafenib, TACE and anti PD1 treatment bulk RNA sequencing cohorts were download from the Gene Expression Omnibus (GEO, <https://www.ncbi.nlm.nih.gov/geo/>) through accessing id GSE109211, GSE104580 and GSE202069. Single-cell RNA-sequencing (scRNA-seq) data of GSE149614 were obtained from GEO [15].

Multi-omics analysis of liver circadian genes

Liver circadian genes (LCGs) were inferred using the cyclic ordering by periodic structure (CYCLOPS) algorithm developed by Ron C. Anafi et al. [16], and they have been compiled into the CircaDB (<http://circadb.hogeneschlab.org/human>) by Pizarro, A et al. [17]. The multi-omics profiles data, including transcriptomic, genomics, and methylation arrays, are all sourced from the paired TCGA-LIHC cohort. The methylation data of TCGA-LIHC cohort are downloaded from XNEA (<https://xen>

a.ucsc.edu/). Similar to the previous study, the methylation probe that shows the strongest negative correlation with mRNA expression was identified as the representative gene methylation probe used in this study [18]. The “maftools” R package was applied to analyze single nucleotide variants (SNVs) of circadian genes. Copy number variation analysis was conducted using GISTIC2, with copy number alterations defined as greater than or equal to 2 or less than or equal to -2. The “ActivePathway” R package [19] was utilized to analyze multi-omics pathway enrichment of LCGs. In brief, we calculated the multi-omics differences between tumor samples and paired normal tissues, and integrated pathway enrichment analysis was performed using the “ActivePathways” function. The merge_method parameter was set to “fisher”, and the cutoff parameter was set to “0.1”. Pathway enrichment was based on the KEGG database and visualized using Cytoscape [20].

Single-cell RNA-sequencing analysis

The downloaded data was processed using R package “Seurat” [21]. After quality control, the data were integrated by “Harmony” method. A total of 30,248 cells (16,093 tumor tissue sourced and 14,155 normal tissue sourced) were analyzed, with an average of 7,735 transcripts detected per cell. We performed dimensionality reduction using Uniform Manifold Approximation and Projection (UMAP). Finally, the cells were annotated by classical markers. The copy number variations and stemness of tumor cells were predicted using R package “inferCNV” and “CytoTRACE” [22]. The R package “Monocle” was used to calculate and visualize the pseudotime developmental trajectories of tumor cells [23]. The EMT signature and Proliferation signature were obtained from the MsigDB database (<https://www.gsea-msigdb.org>) and calculated by the “AUCell” method. For drug prediction analysis, the “Beyondcell” R package were utilized [24].

Spatial transcriptomics data processing

For the ST-seq data analysis, we utilized the “Seurat” R package (v4.1.1). The data, obtained from HRA000437 (<https://ngdc.cncb.ac.cn>) [25], underwent “SCTransform” normalization. Additionally, the expression pattern of RBM17 was visualized using the “SpatialFeaturePlot” function in “Seurat”.

Selecting the key feature of liver circadian genes by machine-learning

To reveal the potential prognosis and molecular mechanism of liver circadian genes (LCGs), we identified the optimal prognostic biomarkers among the LCGs using the LASSO Cox regression model with the “glmnet” R package in the TCGA-LIHC cohort. To select the most suitable lambda value and avoid overfitting, we applied

ten-fold cross-validation. A total of 10 LCGs with non-zero coefficients were selected through 10-fold cross-validation. Random Forest is a versatile and accessible machine-learning algorithm often used for classification and regression tasks. As it has no restrictions on variable conditions, it has higher accuracy, sensitivity, and specificity than decision trees in predicting continuous variables and obtains predictions without significant bias [26]. Here, we used the R Package Random Forest to screen for the most significant LCGs associated with prognosis. Default parameters were used as they consistently produced stable results: ntree=500. A total of the top 10 LCGs were selected based on the rank of “MeanDecreaseAccuracy”. Finally, by combining Random Forest and Lasso regression, we took the intersection of the 2 subsets of feature genes selected from the above methods to ultimately determine the key feature genes.

Construction of circadian prognosis scores (CPS)

The circadian prognosis scores (CPS) were constructed using regression coefficients based on IL18RAP, GNL2, RBM17, ZDHHC18. The CPS was formulated as follows:

$$\text{CPS} = \sum_i \text{Coefficient}(i) \times \text{Expression}(i)$$

Patients were stratified into high and low CPS groups based on the median CPS. The Kaplan-Meier method was employed to assess differences in survival between the high- and low-CPS groups. Additionally, time-dependent receiver operating characteristic (ROC) curve analysis was conducted to evaluate the accuracy of the CPS in predicting TCGA-LIHC prognosis. The robustness of the CPS was further validated in the ICGC cohort.

Pathway-enrichment and immune infiltration analysis

For pathway enrichment, gene sets were obtained from the MsigDB database (<https://www.gsea-msigdb.org>). The “GSVA” R package was applied to calculate pathway enrichment characteristics for single samples. The “IOBR” R package serves as an integrated tool for TME analysis [27]. The immune infiltration was computed using the “deconvolve_tme” function of the “IOBR”. Specific parameters were set to their default values without any modifications. Additionally, the MHC signature was obtained from the “IOBR”. These signatures were employed in estimating the relative scores for each sample using the “GSVA” method.

Clinical samples

A total of 112 HCC tissue samples were collected with informed consent from patients who underwent hepatectomy at the Sun Yat-Sen University Cancer Center (Guangzhou, China). Complete clinic pathological and

follow-up data were available, and patient demographic information is provided in Supplementary Table S1. The use of clinical specimens in this study was approved by the Committee for Ethical Review of Research Involving Human Subjects at the Sun Yat-Sen University Cancer Center.

Immunohistochemistry (IHC) staining

Immunohistochemistry (IHC) analysis was performed using a primary antibody against RBM17 (1:200 dilution, Cat#13918-1-AP, Proteintech). The IHC staining followed standardized protocols as described elsewhere [28]. Each sample was scored as 1 (negative), 2 (weak positive), or 3 (strong positive) based on the relative staining intensity. Samples exhibiting strong positivity were classified as the high expression group, while negative and weakly positive samples were categorized into the low expression group.

Immunofluorescence staining

The cell slides were fixed with 4% paraformaldehyde, then were pre-incubated with 10% normal goat serum at room temperature for 30 min to reduce nonspecific reaction. Subsequently, the slides were incubated with rabbit monoclonal anti-CD133 (1:200 dilution), for 12 h at 4 °C. The slides were incubated with a secondary antibody (fluor 488 labeled) for 1 h at room temperature and stained with DAPI for 5 min. The proportion of CD133+ cells was calculated by counting the number of CD133-positive cells in randomly selected regions of the slide. The total number of cells was determined by counting DAPI-stained nuclei in the same regions. The ratio of CD133+ cells was calculated as the number of CD133-positive cells divided by the total number of cells in each field.

Cell culture

The HCC cell line *PLC-8024* (*CRL-8024*) and HepG-2 were acquired from the Institute of Virology of the Chinese Academy of Sciences (Beijing, China). 293T cells were obtained from National Collection of Authenticated Cell Cultures, Shanghai, China. All cell lines were authenticated by short tandem repeat profiling and routinely tested for the absence of mycoplasma contamination. Specifically, we used a PCR-based mycoplasma detection kit (GMyc-PCR Mycoplasma Test Kit, Cat#40601ES10, Yeasen) to test the cell culture supernatant at regular intervals. The cells were cultured in Dulbecco's modified Eagle's medium (DMEM) (Gibco), supplemented with 10% fetal bovine serum (Gibco) and 1% penicillin/streptomycin mixture (Gibco). All cell lines utilized in this investigation were incubated at 37 °C in a humidified incubator maintained at 5% CO₂.

Plasmids, lentivirus production and cell infection

The RBM17-shRNA expression vectors and the scrambled shRNA control were constructed with the pLL3.7 plasmid (Addgene). The RBM17-shRNA target sequence is GATGAAGCAGTACGGATATTT. Virus was made by co-transfecting the pLL3.7 constructs along with helper plasmids from the Directional TOPO Expression Kit (Invitrogen) into 293T cells using HieffTrans Liposomal Transfection Reagent (Yeasen Biotech) according to the manufacturer's recommendations. After transfection for 72 h, the viral supernatant was collected and used to infect the cell line. Subsequently, stable knockdown cell lines were obtained by further selection with puromycin (Gibco).

Cell viability assay and foci formation

Cells were seeded into 96-well plates at a density of 2000 cells per well in 100 µl of growth medium. Subsequently, 10 µl of CCK8 solution (Cat# HY-K0301, MCE) was added to each well, followed by incubation at 37 °C for 3 h. The optical density was measured at a wavelength of 452 nm using a microplate reader over a period of 5 days. Triplicate repeats were performed to evaluate variance and statistical significance. The data points were represented as the average of triplicate wells. As for foci formation, cells were plated in 6 well plate. 7–12 days later cells were washed with PBS three times, fixed with 75% ethanol for 30 min, and dyed purple by gentian violet. The colony formation rates were calculated by dividing the number of foci by the total number of cells initially seeded, expressed as a percentage.

Transwell and wound healing assay

For the migration assay, $2 \sim 5 \times 10^4$ cells were suspended in 100 µL DMEM and plated onto the upper chamber (Corning) inserts. Meanwhile, 700 µL DMEM supplemented with 10% FBS was added to the lower chamber in a 24-well plate. After 48-hour incubation at 37 °C, the migrated cells were fixed and dyed. For the invasion assay, chambers were uniformly covered with 60 µL Matrigel (Cat# 354234, BD Biosciences) diluted with DMEM (1:8). After 2-hour incubation at 37 °C, cell suspension was plated onto the upper chamber, with 700 µL DMEM supplemented with 10% FBS adding to the lower chamber. Finally, the invasive cells were dyed. For the wound healing assay, $2 \sim 5 \times 10^4$ cells were plated onto 6-well plates. When the confluence was up to 90%, the cell monolayer was scratched with a 1 mL pipette tip. After removing detached cells, the remaining cells were cultivated in medium without FBS. Cellular migration was quantified using Image J.

Sphere formation assay

Cells were plated as single cells into 96-well plates at 100 cells/well with 2 mL DMEM/F12 (Hyclone) containing 1% B27 supplement (Thermofisher), 1% N2 supplement (Thermofisher), 20 ng/mL EGF (Thermofisher) and 10 ng/mL bFGF (Thermofisher). After 7 days of growth, spheres were counted. Sphere formation rate = sphere-formed cells/seeded cells.

Western blot

Samples were lysed with Pierce RIPA buffer (Thermo Fisher Scientific, USA) and quantified using Bio-Rad Protein Assay (Bio-Rad). After being mixed with loading dye (Bio-Rad), the protein was denatured (100°C, 15 min). Denatured proteins were separated by SDS-PAGE and transferred onto a PVDF membrane (Millipore, USA). After blocking for 1 h, the membranes were incubated with primary antibodies (RBM17, Cat# 13918-1-AP, Proteintech; GAPDH, Cat# 2118, CST; CDK2, Cat# 2546, CST; CyclinE2, Cat# 4132, CST; CD133, Cat# 18470-1-AP, Proteintech) and then incubated with peroxidase-conjugated secondary antibodies. Immunoreactive bands were visualized using ECL (Bio-Rad) and exposed to autoradiograph film.

Cell cycle and apoptosis flow cytometry

Cells were grown to a density of 70% in 6-well dishes and collected for staining with propidium iodide (PI, Cat# A601112-0100, Sangon) according to the manufacturer's instructions. For the apoptosis assay, the Annexin V-Alexa Fluor 488/7-AAD Cell Apoptosis Detection Kit (Cat# 40313ES50, Yeasen Biotech) was utilized, and the procedures were conducted according to the manufacturer's instructions. A CytoFLEX cytometer (Beckman Coulter) was used to measure changes in cell cycle. FlowJo was utilized to analyze the generated flow cytometry data.

Animal experiment

The Institutional Animal Care and Use Committee at Southern University of Science and Technology has reviewed and approved all animal experiments. Four-to five-week-old male BALB/c-nu/nu mice were reared under specific pathogen-free conditions at the Laboratory Animal Centre of Southern University of Science and Technology. Afterwards, the mice were randomly divided into four groups (nc, nc + Cisplatin, shRBM17, shRBM17 + Cisplatin). In the drug resistance assay, PLC-8024 cells stably transfected with lenti-sh-RBM17 or lenti-sh-NC were injected subcutaneously into BALB/c-nu/nu mice (4 × 10⁶ cells, 5 mice per group). When the tumor volume reached approximately 50 mm³. Mice were treated with cisplatin (3 mg/kg every three days, intraperitoneally), while control mice were treated with saline.

Tumor size was measured every 3 days. Tumor volume was estimated using the formula: $V = \text{length} \times \text{width}^2/2$. All mice were housed under a controlled 12-hour light/12-hour dark cycle. Euthanasia was performed during the standard daytime working period.

Statistical analysis

Data processing, analysis, and visualization were carried out using R packages (version 4.30; <https://www.bi.oconductor.org/>) or Graphpad Prism software (version 8.0.1; <https://www.graphpad.com/>). To compare differences between two groups, we employed Student's t-test or Mann-Whitney U test. Correlation analysis between variables was performed using Pearson or Spearman test. Survival analysis was conducted utilizing the Kaplan-Meier approach and log-rank test, with the survival and "Survminer" packages. Uni- and multivariable Cox regression models were constructed to compute hazard ratios (HRs) and identify independent prognostic factors. A significance level of $P < 0.05$ was considered statistically significant. Results are expressed as the mean ± standard error of the mean.

Results

Multi-omics analysis reveals dysregulation of liver circadian genes in liver cancer

Our overall research workflow is presented in (Fig. 1A). A total of 378 Liver circadian genes (LCGs) were gathered from CircaDB, which are genes rhythmically expressed in the normal liver. Transcription profiles of 378 LCGs showed extensive disruption in liver tumors compared with normal livers from the TCGA-LIHC dataset (Fig. 2A). We integrated multi-omics data to investigate whether genetic, epigenetic, and transcriptional regulation contributes to the disordered expression of LCGs. Genetic mutations of LCGs are not frequent (less than 5%) in liver cancer, as illustrated in (Fig. 2B). Regarding copy number variation (CNV) characteristics, a considerable portion of LCGs displayed prevalent copy number amplifications (Fig. 2C). Methylation characteristics of LCGs were also investigated. The top 15 genes with upregulated methylation and the top 15 genes with downregulated methylation in tumors were visualized (Fig. 2D). Multi-omics correlation analysis reveals a complex interplay in the dysregulation of LCGs. The overall methylation associated with LCGs expression shows a negative correlation, while a positive correlation is observed with copy number variations. BMAL1, CLOCK, NR1D1 and NR1D2 are considered as core transcription factors in circadian regulation [29–32]. Their expression levels positively correlate with the overall LCGs expression, with CLOCK demonstrating the strongest correlation among them (Fig. 2E). Multi-omics integration pathway enrichment analysis indicates that dysregulation

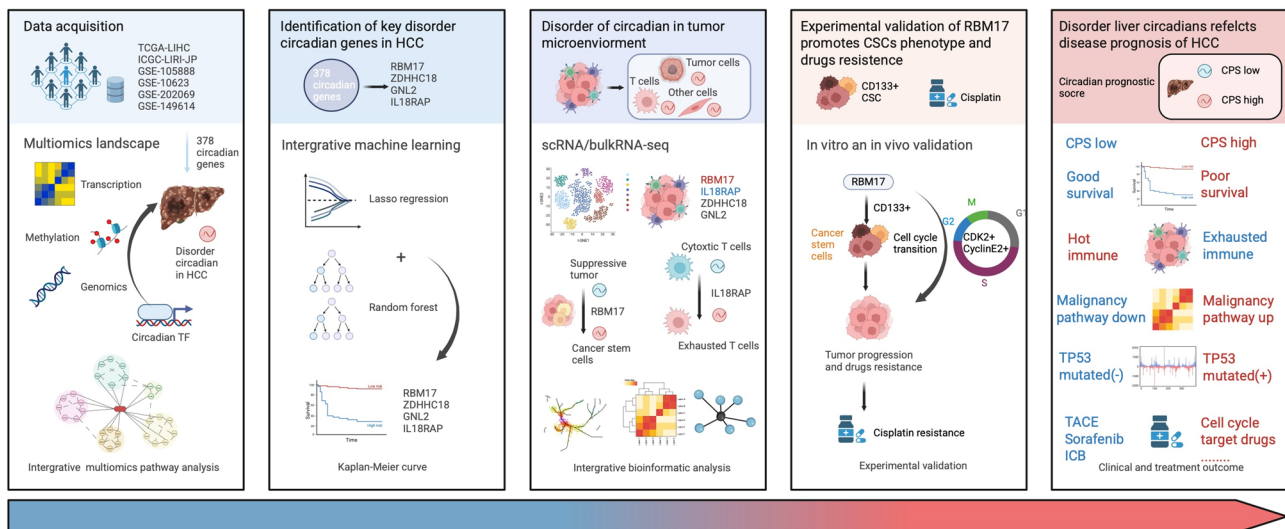


Fig. 1 Overall research workflow of this study. (A). The flowchart of the study. TF, Transcription factor; LCGs, Liver circadian genes; TME, Tumor microenvironment; CSC, Cancer stem cell; TCGA, The Cancer Genome Atlas; ICGC, International Cancer Genome Consortium

of LCGs is associated with pathways of cancer, cell proliferation, metabolism, endothelium-interstitial transition, innate immunity, and adaptive immunity. LCGs mRNA dysregulation plays a predominant role in most pro-malignant pathways (Fig. 2F and Supplementary Table S2).

Identifying critical LCGs for liver cancer prognosis using machine learning

Given the extensive crosstalk between LCGs disruption and pro-malignant pathways, we further employed machine learning techniques to identify LCGs associated with liver cancer prognosis. The Random Forest algorithm and LASSO regression are two machine-learning techniques used for identifying the most significant predictors in a dataset. Our approach combined these two algorithms to enhance the representativeness and stability of feature selection. Ultimately, IL18RAP, RBM17, GNL2, and ZDHHC18 were pinpointed as the most pivotal dysregulated circadian genes in predicting liver cancer prognosis (Fig. 3A). Kaplan-Meier curves reveal ZDHHC18, GNL2, and RBM17 as adverse prognostic factors in liver cancer, while IL18RAP emerges as a favorable prognostic factor in both TCGA and ICGC cohorts (Fig. 3C). Consistently, ZDHHC18, GNL2, and RBM17 exhibit significant upregulation in tumor tissue compared to the normal bulk gene expression level, while IL18RAP shows downregulation (Fig. 3B).

Dissecting critical LCGs activities in tumor microenvironment using single-cell RNA transcriptome

To further dissect the activities of LCGs in various cellular compositions within the tumor microenvironment of liver cancer, we carried out scRNA-seq analysis. After

implementing quality control measures, we integrated scRNA-seq data from ten tumor tissues and eight paired normal liver tissues obtained from the GSE149614 dataset (Supplementary Figure S1A). The cells were then annotated as “B cells” (B), “Fibroblasts” (Fibro), “Endothelial cells” (Endo), “Hepatocytes”, “Myeloid cells” (Myeloid), and “T/NK cells” (T/NK) (Fig. 4A-B and Supplementary Figure S1B). In exploring the expression of four key LCGs within the tumor microenvironment, we noted a widespread upregulation of RBM17 and GNL2 in tumor-sourced hepatocytes. RBM17 was also found to be enriched in tumor-derived B cells and fibroblasts. However, no significant changes were observed in myeloid and endothelial cells from different tissue sources, suggesting that RBM17 may exert a potentially tumor-promoting effect in certain cell types (Fig. 4C). Despite the low expression levels of ZDHHC18 and IL18RAP on a single-cell basis, likely due to dropout, our analysis identified specific expression pattern of IL18RAP in T/NK cells, especially those from normal tissues (Fig. 4D and Supplementary Figure S1C). Given the pivotal role of T cells in the tumor microenvironment, we subclustered T/NK cells for further investigation (Supplementary Figure S1D). This led to the clustering of T cells into several subsets: cytotoxic CD8 T cells, exhausted CD8 T cells, T regulatory cells (Tregs), naive T cells, CD4 T cells, natural killer (NK) cells, and a small fraction of other cells (Fig. 4E). Notably, a significant upregulation of IL18RAP was observed in cytotoxic CD8-GZMK cells and, to a lesser extent, in NK cells (Fig. 4F). This suggests a potential role of IL18RAP in enhancing immune surveillance. Supporting our hypothesis, our bulk RNA-Seq analysis showed a significant positive correlation between

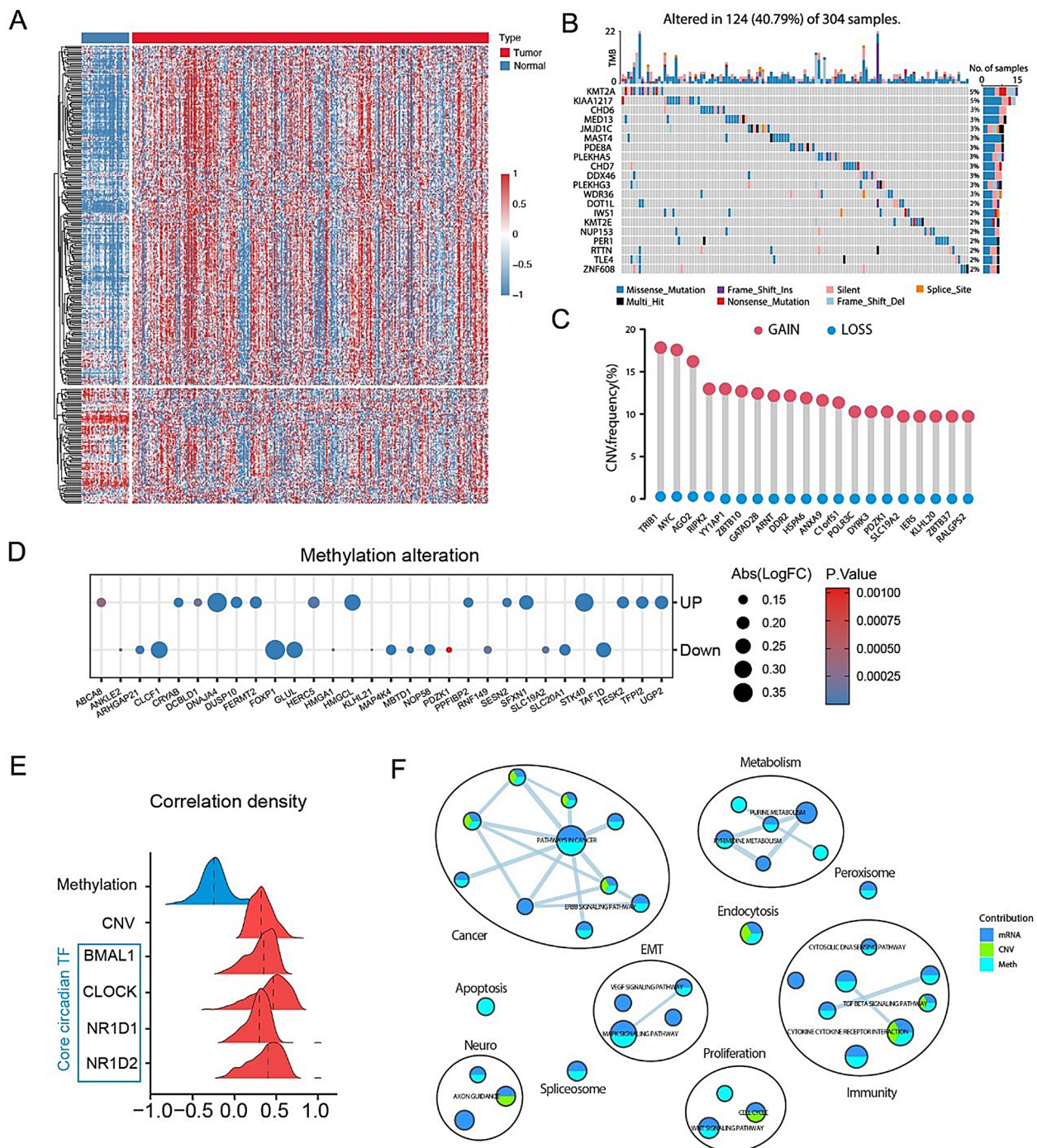


Fig. 2 Multi-omics analysis reveals dysregulation of liver circadian genes in liver cancer. **(A)** Expression heatmap of 378 LCGs in TCGA-LIHC datasets. **(B)** Mutations of LCGs in the TCGA-LIHC cohort. Each column corresponds to an individual sample, and each row to a specific genes. Mutation type is indicated by a distinct color. **(C)** CNV variant frequencies of LCGs in TCGA-LIHC. The height of the column represents the frequency of change. **(D)** The dotplot of alterations in LCGs methylation. **(E)** The ridge plot depicting the multi-omics correlation of circadian genes. Blue indicates a negative correlation, red indicates a positive correlation, and the dashed line marks the median correlation. **(F)** The ActivePathway enrichment plot for dysregulated LCGs. Node size represents the number of genes enriched in the pathway, while node color corresponds to the respective omics dimension. CNV, Copy number variation; TF, Transcription factor

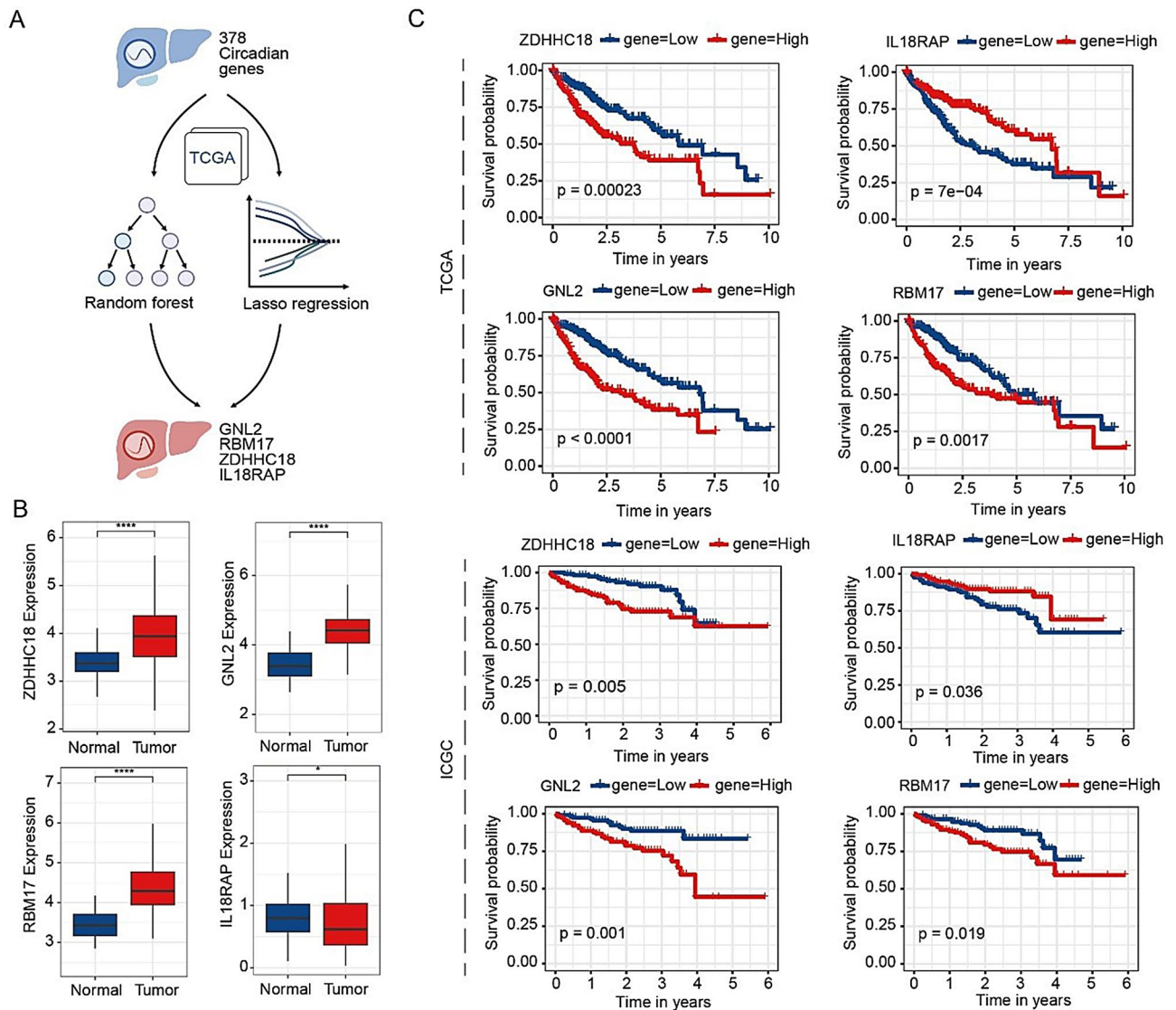


Fig. 3 Identifying critical LCGs for liver cancer prognosis using machine learning. **(A)** The strategy for selecting key LCGs using machine learning. **(B)** Box plots of gene expression in TCGA adjacent normal and tumor tissues. **(C)** The responding Kaplan-Meier curve for ZDHHC18, IL18RAP, GNL2, and RBM17. The first four figures correspond to results obtained from the TCGA dataset, while the next four figures pertain to results from the ICGC cohort. The Kaplan-Meier curves were analyzed using the log-rank test. TCGA, The Cancer Genome Atlas; ICGC, International Cancer Genome Consortium

IL18RAP and immune-related pathways, as well as with CD8T/NK cells (Supplementary Figure S1E).

Multi-omics analysis and experimental validation unravel the pro-malignant role of RBM17 in liver cancer

The gene RBM17 was selected for further exploration due to its significantly increased expression in tumor-sourced hepatocytes. We initially confirmed the significant upregulation of RBM17 in leading-edge section, tumor section, and portal vein tumor thrombus section in publicly available spatial transcriptomic slices. (Supplementary Figure S2A). Subsequent immunohistochemical (IHC) staining validated the significant association

between RBM17 expression and worse overall survival in our in-house HCC cohort. (Fig. 5A). We then examined the expression of RBM17 across different tumor-sourced hepatocyte clusters using public scRNA-seq data [15]. The hepatocytes were subgrouped into 10 clusters, with RBM17 showing the most significant upregulation in cluster 2 (Fig. 5B and Supplementary Figure S2B). The inferCNV tool was utilized to calculate the copy number variation (CNV) scores for the various tumor clusters (Figure S2C). The findings revealed that cluster 2 exhibited a high CNV score, which is frequently linked to tumor malignancy. The epithelial-mesenchymal transition (EMT) score and proliferation capability were

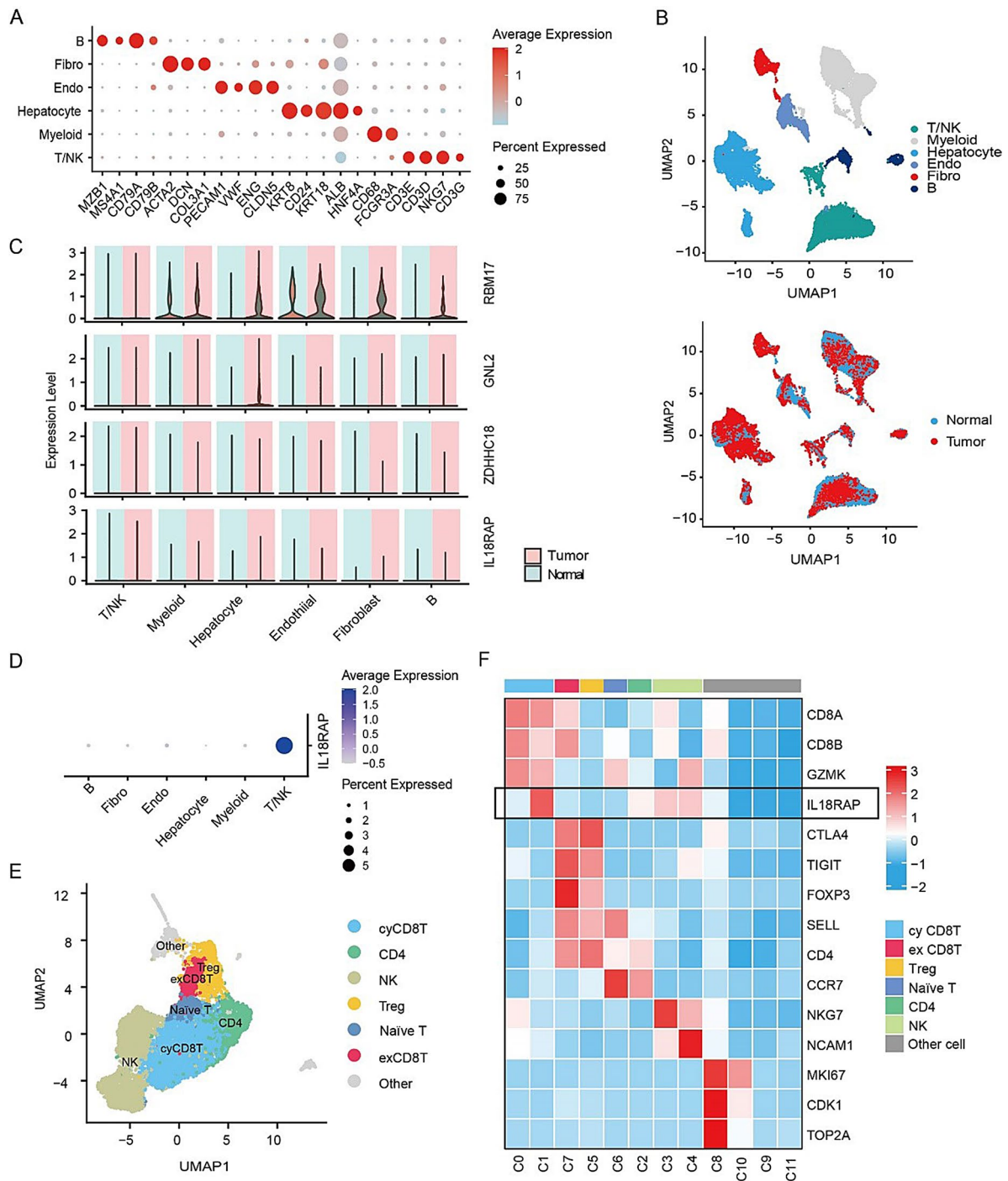


Fig. 4 Dissecting critical LCG activities in tumor microenvironment using single-cell RNA transcriptome. **(A)** Dotplot of marker gene expression in different cell types. **(B)** UMAP graph of cell types and sample sites. **(C)** Expression violin-plot of core circadian prognostic genes, with green indicating adjacent normal tissues and red indicating tumor samples. **(D)** Expression Dotplot of IL18RAP in different cell types. **(E)** UMAP graph of different T cell subtypes. **(F)** Gene relative expression heatmap of different T cell sub-cluster. cyCD8T, cytotoxic CD8T cell; ex CD8T, exhausted CD8T cell; Treg, regulatory T cell; NK, Natural killer cells; B, B cell; Endo, Endothelial cell

assessed using the AUCells method. Consistently, cluster 2 showed the highest scores among the 10 tumor clusters (Fig. 5C). The Monocle pseudotime analysis further revealed that cluster 2 resides at the trajectory endpoint,

indicating a progressive increase in RBM17 expression along tumor progression (Fig. 5D). In the bulk RNA sequencing level, single sample gene set enrichment analysis (ssGSEA) was conducted in the TCGA-LIHC cohort,

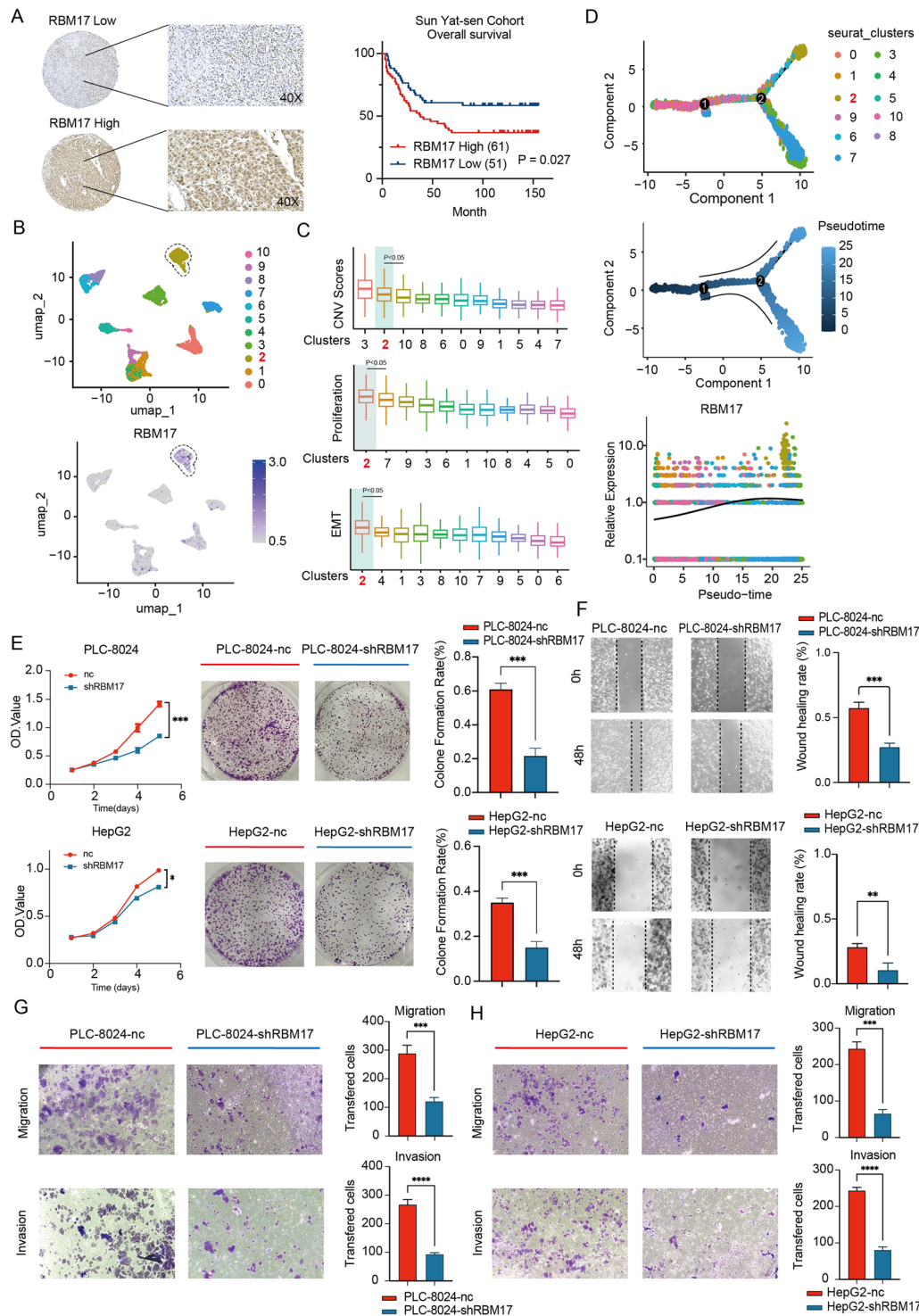


Fig. 5 (See legend on next page.)

which revealed a significant positive correlation between RBM17 expression and pathways regulating cell proliferation, stemness, and EMT (Supplementary Figure S2D). In view of the above evidence, the necessity of RBM17 for the malignant functions of liver cancer cells was further examined. In vitro experiments demonstrated

that shRNA-mediated silencing of RBM17 reduced cell viability and the frequency of foci formation in human HCC cell lines PLC-8024 and HepG2 (Fig. 5E). In addition, wound healing assays and transwell experiments revealed that knocking down RBM17 significantly inhibited the (EMT) phenotype in PLC-8024 and HepG2 cells

(See figure on previous page.)

Fig. 5 Multi-omics analysis and experimental validation unravel the pro-malignant role of RBM17 in liver cancer. **(A)**. Representative images of immunohistochemistry (IHC) staining showing high and low expression levels of RBM17 in tumor tissues of HCC (left panel). The Kaplan–Meier curve of different RBM17 expression groups (right panel). The Kaplan–Meier curves were analyzed using the log-rank test ($n=112$). **(B)**. UMAP graph of subsetted tumor cell clusters (Top panel). Dimplot of RBM17 expression level (Bottom panel). **(C)**. Boxplots of the CNV scores, EMT scores, and proliferation scores across different clusters. **(D)**. Monocle pseudo-temporal plot. The top panel represents the pseudo time. The middle panel illustrates the positions of different cell clusters within the pseudo trajectory, with the C2 cluster (high RBM17 expression) located at the trajectory's terminus. The bottom panel represents the relative expression levels of RBM17 in pseudo time. **(E)**. Cell proliferation curve by cck8 assay (left panels, $n=3$) and foci formation assay (right panels, $n=3$). **(F)**. Representative image of wound healing assay of the indicated cells. The corresponding barplot on the right illustrates the wound healing rate(%). **(G)**. Representative image of transwell assay of PLC-8024 ($n=3$). **(H)**. Representative image of transwell assay of HepG-2 ($n=3$). * $P < 0.05$, ** $P < 0.01$, *** $P < 0.005$, **** $P < 0.001$, The data are presented as the means \pm standard deviations (SD) of three independent experiments. The P value was determined using the student t-test

(Fig. 5F–H). In summary, the analyses and experiments consistently demonstrate the significant role of RBM17 in liver cancer progression.

RBM17 regulates the cancer stem cell properties in liver cancer

Previous studies have suggested an association between disrupted circadian rhythms and cancer stem cells (CSCs) [33]. Our multi-omics analysis also revealed a correlation between RBM17 and liver cancer stemness and differentiation. Next, we aim to investigate whether RBM17 affects the stemness of liver cancer cells. CytoTRACE analysis showed a significant overlap between RBM17 expression and poorly differentiated cells, suggesting an association between RBM17 and CSCs (Fig. 6A). Furthermore, analysis of CSC signature based on TCGA-LIHC cohort revealed that patients with high RBM17 expression had higher mRNA stemness index (mRNAsi) scores ($P < 0.01$), indicating increased stemness (Fig. 6B). Based on these results, we hypothesize that RBM17 may help in regulating the stemness of tumor cells. In support of this, spheroids formation assays demonstrated that silencing RBM17 significantly reduced the number of spheroids formed by CSCs (Fig. 6C). Pseudo-bulk analysis of RBM17 highly-expressing cells revealed the upregulation of many CSCs markers, including CD133 (Fig. 6D). Consistently, the protein expression level and immunofluorescence signals of CD133 were significantly reduced after RBM17 depletion (Fig. 6E–F). CSCs exhibit high proliferative properties. Flow cytometry analysis revealed that the loss of RBM17 led to cell cycle arrest at the G1 phase, accompanied by reduced expression of G1 phase-promoting proteins CDK2 and Cyclin E2 (Fig. 6G–H). Overall, these results underscore the critical role of RBM17 in maintaining CSCs and consequently promoting the progression of liver cancer.

RBM17 suppression enhances cisplatin sensitivity in liver cancer

Drug resistance is a defining characteristic of cancer stem cells (CSCs) [34]. Given RBM17's essential role in maintaining cancer stemness, we explored its relationship with drug resistance. Using the “Beyondcell” algorithm,

we predicted the heterogeneity in drug responses of liver cancer cells to cisplatin and sorafenib at the single-cell level. Our findings revealed that cells expressing high levels of RBM17 significantly overlapped with those exhibiting resistance to cisplatin (Fig. 7A–B). This was illustrated by a notable increase in the BSC values for cisplatin resistance in tumor cells with high RBM17 expression, in comparison to other tumor cells. However, no significant variance was observed in response to sorafenib between the two cell groups (a higher BSC value indicates greater drug resistance) (Fig. 7B). In addition, the “Oncopredict” tool was employed to predict the sensitivity of various patients to these drugs, based on data from the TCGA-LIHC cohort. Within this cohort, RBM17 expression levels were positively correlated with the IC50 values of sorafenib ($R=0.28$) and cisplatin ($R=0.52$) (Fig. 7C), suggesting a potential involvement of RBM17 in liver cancer drug resistance. Furthermore, analyses based on the TACE cohort consistently demonstrated that RBM17 serves as a predictive marker for chemotherapy drug response (Fig. 7D). It is noteworthy that our results consistently demonstrate a significant association between RBM17 expression and cisplatin resistance across different computational methods. In vitro assays showed that RBM17 depletion reduced the survival of PLC-8024 and HepG-2 cell lines across various cisplatin concentration gradients (Fig. 7E). Apoptosis analysis further demonstrated that knocking down RBM17 significantly enhanced cisplatin-induced apoptosis in PLC-8024 ($P < 0.001$) (Fig. 7F). To corroborate the role of RBM17 in drug resistance in vivo, we established a cell line-derived xenograft (CDX) in nude mice. Consistent with our in vitro findings, RBM17 knockdown markedly inhibited tumor growth and amplified the inhibitory effects following cisplatin treatment in vivo. (Fig. 7G).

Development of circadian prognosis scores to enhance liver cancer prognosis prediction

We explored the substantial correlation between the dysregulation of four circadian genes, notably RBM17, and the prognosis of liver cancer. To quantitatively evaluate the prognosis of liver cancers, we devised the circadian prognosis score (CPS). The CPS distribution and survival

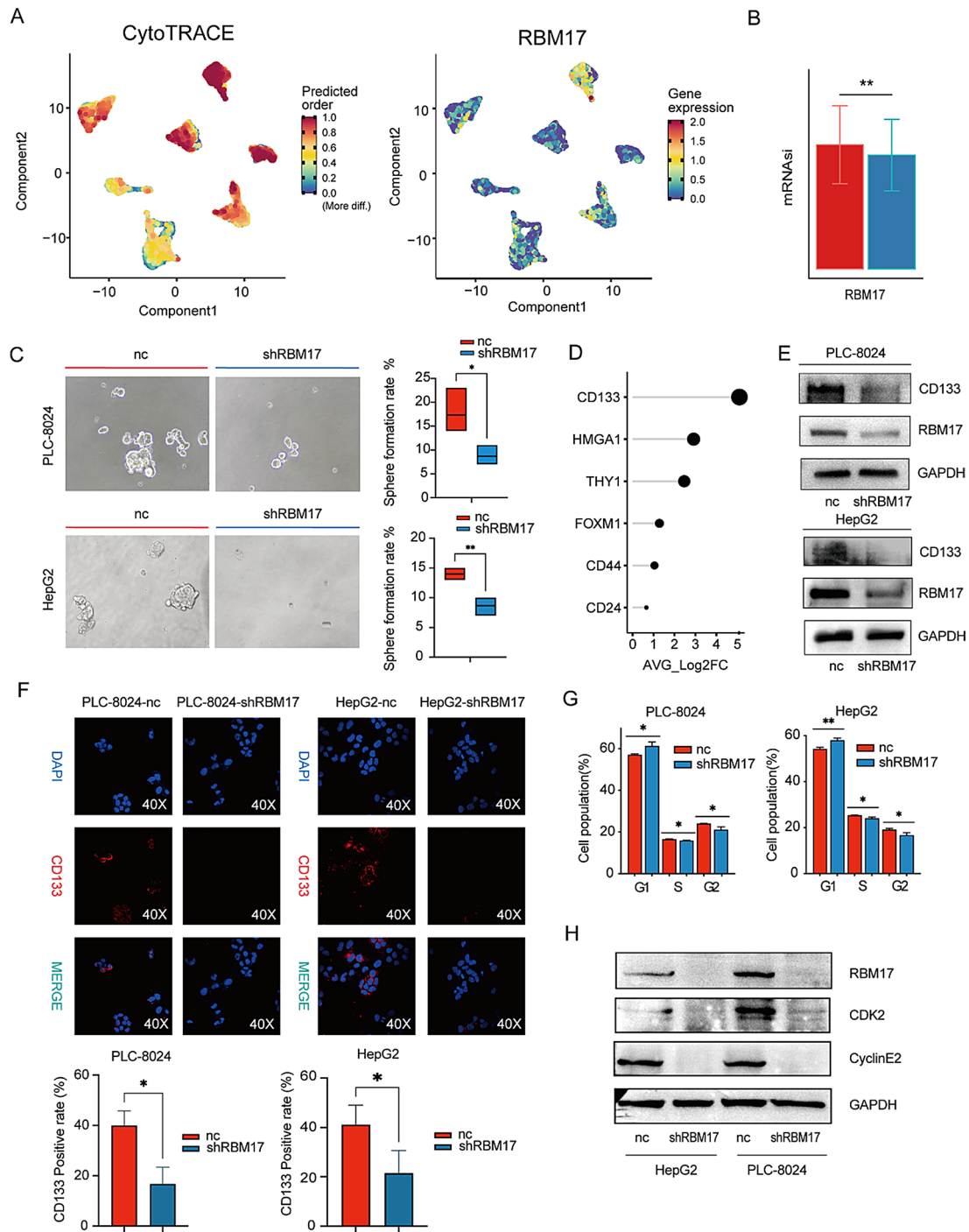


Fig. 6 RBM17 regulates the cancer stem cell properties in liver cancer. **(A)** UMAP plot of CytoTRACE predicted cell order (more to less differentiated), indicated by color from blue to red (left panel). UMAP plot of RBM17 expression levels (right panel). **(B)** Boxplot of mRNA stemness index (mRNAsI). **(C)** Representative image of spheroids formed assay and quantification of the indicated cells. **(D)** Lollipop plot of CSCs marker fold change. **(E)** Inhibition of CD133 by RBM17 silencing was verified by western blotting of the indicated cells. GAPDH was used as the loading control. **(F)** Immunofluorescence analysis of CD133 expression in PLC-8024 and HepG-2 cells. The nuclei were stained with DAPI (blue). **(G)** Flow cytometry detection of cell cycle using PI staining in PLC-8024 and HepG-2 ($n=3$). **(H)** RBM17 and G1/S-related proteins, including CyclinE2, CDK2 were detected with WB. * $P < 0.05$, ** $P < 0.01$, *** $P < 0.005$, **** $P < 0.001$. The data are presented as the means \pm standard deviations (SD) of three independent experiments. The P value was determined using the student t-test

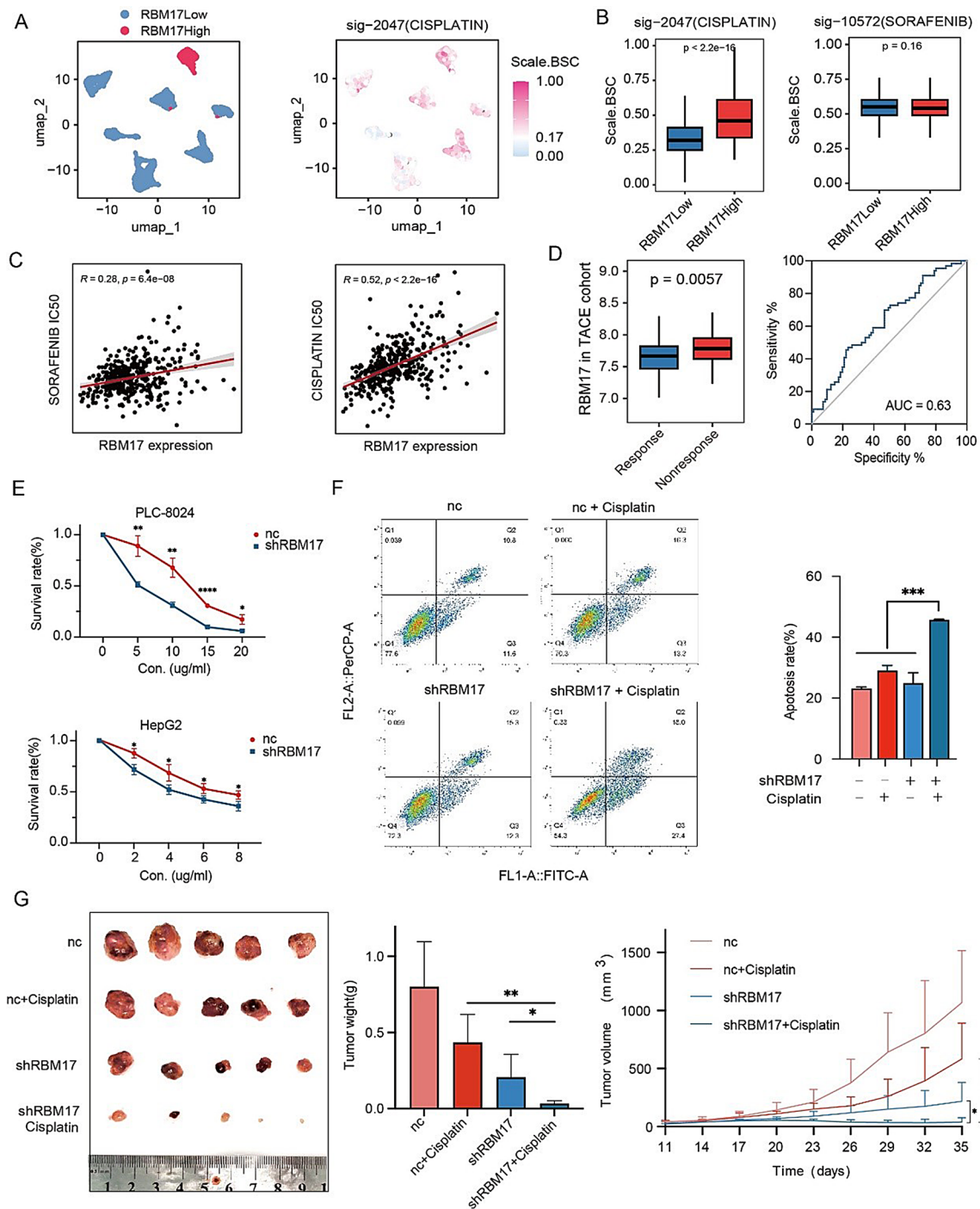


Fig. 7 RBM17 suppression enhances cisplatin sensitivity in liver cancer. **(A)** UMAP plot of tumor cells and the definite cell population (left). UMAP plot for BCS Score mapping. The red color reflects resistance to Cisplatin (right). **(B)** Boxplot of BCS value in different RBM17 status cell groups. **(C)** Scatter plot of the correlation between predicted IC50 and the expression of RBM17. **(D)** Boxplot of RBM17 expression in different TACE response groups (left). The Area Under Curve (AUC) of RBM17 reflects the TACE response. **(E)** The survival curves based on the CCK8 assay ($n=3$). **(F)** Flow cytometry apoptosis analysis depicting the enhancement of cisplatin-induced apoptosis in PLC-8024 following RBM17 silencing ($n=3$). **(G)** Photos of excised subcutaneous Cell line-derived xenograft tumors and quantification of tumor weight and volume. $*P < 0.05$, $**P < 0.01$, $***P < 0.005$, $****P < 0.001$. The data are presented as the means \pm standard deviations (SD) of three independent experiments. The P value was determined using the student t-test

status across in TCGA and ICGC cohorts were delineated in the top panel (Fig. 8A). For the TCGA cohort, the average AUC values for 1-year, 3-year, and 5-year prognosis predictions were 0.77, 0.72, and 0.70, respectively (Fig. 8A). Correspondingly, for the ICGC cohort, the average AUC values for 1-year, 2-year, and 3-year survival were found to be 0.73, 0.71, and 0.70, respectively (Fig. 8A). To augment the practical applicability of the CPS, we amalgamated independent prognostic factors and formulated a nomogram. This nomogram serves as a quantitative instrument, enabling clinicians to ascertain the mortality risk associated with liver cancers (Fig. 8B). The calculation of a total score for each patient is achieved by summing the scores attributed to each prognostic parameter. It is noted that a higher total score is indicative of a worse prognosis for the patient. Kaplan-Meier curves elucidated the superior survival discrimination capability across distinct NomoRisk categories (Fig. 8C). Additionally, a calibration plot affirmed that the performance of the nomogram closely parallels that of an ideal model (Fig. 8D), further validating its efficacy and reliability in the clinical prognosis of liver cancer.

Different genomic mutation landscapes and tumor-associated pathways among high- and low-risk groups

We further explored the molecular and cellular characteristics of the two different risk groups defined by CPS. It is well-established that genomic mutations are pivotal in the initiation and progression of tumorigenesis [35]. Analysis of the single-nucleotide variation (SNV) landscape revealed distinct gene mutation profiles of different CPS populations (Fig. 9A). Notably, the mutation frequencies of TP53, along with SP1 and RESF1, were found to be higher in patients with high CPS, while TOGA-RAM2 showed a higher mutation frequency in patients with low CPS ($P < 0.01$) (Fig. 9B). Specifically, the TP53 gene, a critical tumor suppressor gene, showed mutations in 79 out of 182 patients with high CPS, while only 20 out of 179 patients with low CPS exhibited mutations ($P < 0.005$) (Fig. 9B). Mutation site analysis uncovered extensive alterations in the TP53 gene body region among individuals with high CPS, including the hotspot mutation R249S (Fig. 9C). Additionally, co-mutation analysis revealed a widespread co-occurrence of mutations among individuals within the high CPS group (Fig. 9D). Similarly, copy number variation analysis indicated that the high CPS group exhibited more copy number amplifications (CNA) and loss of heterozygosity (LOH). Pathway enrichment analysis identified distinct pathway enrichment features in individuals with high CPS, implicating DNA replication, cell cycle regulation, DNA damage repair, and metabolism (Fig. 9F). In conclusion, these results highlight significant disparities in gene mutations and pathway activation among different CPS populations,

offering valuable insights into the potential roles of circadian gene dysregulation in liver tumorigenesis.

Distinct immune microenvironments and responses to therapy among high- and low-risk groups

An increasing body of research highlights a significant interplay between circadian rhythms and the tumor immune microenvironment (TME). To investigate the association between CPS and TME, we employed a comprehensive approach, integrating algorithms such as EPIC, MPC, IPS, xCell, and Estimate, to generate detailed immune infiltration profiles for different CPS subgroups (Fig. 10A). The results revealed pronounced immune cell infiltration in the low CPS subgroup, in contrast to the observed immune exhaustion within the high CPS subgroup. Furthermore, the MHC signature, as determined through GSVA, demonstrated elevated levels in the low CPS populations, indicative of enhanced immune functionality (Fig. 10B and C). These findings suggest that a low CPS is associated with a “hot” immune subtype, characterized by with robust immune activity, which may be more amenable to immunotherapy. Supporting this hypothesis, our analysis utilizing the TIDE algorithm identified patients likely to respond to immunotherapy, who predominantly exhibited lower CPS values. A notable positive correlation was established between CPS and TIDE score, with a higher TIDE score suggesting a decreased likelihood of benefiting from immunotherapy ($R = 0.42$) (Fig. 10D-F). Employing CPS to differentiate immunotherapy response yielded an AUC value of 0.65 (Fig. 10G). Consistency in these findings was further validated in a cohort of liver cancer patients treated with anti-PD-1 therapy (Supplementary Figure S3A). These results indicate that CPS defines distinct immune subtypes and may be used to guide immunotherapy decisions. Despite the promising potential of immunotherapy for treating liver cancer, sorafenib and TACE therapy remain the mainstream treatment modalities. Analysis of patient cohorts undergoing sorafenib treatment revealed a significant increase in CPS among non-responders, with an AUC value of 0.88 for sorafenib response prediction. Similarly, within cohorts receiving TACE therapy, non-responders exhibited elevated CPS levels, with an AUC value of 0.70 for response prediction (Fig. 10H-I). To identify potential therapeutic agents for high CPS patients, the GDSC2 datasets and “Oncopredict” algorithm were employed to ascertain the correlation between CPS and sensitivity to a panel of 192 drugs. Subsequent ranking identified 10 drugs with a correlation coefficient (“Rho”) less than -0.4 , indicating potential efficacy. These agents include ML323_1629, Sepantromium, Tozasertib, BMS.345541_1249, MK.1775_1179, Daporinad, Ulixertinib, Paclitaxel, GDC0810_1925, and Wee1.Inhibitor_1046 (Fig. 10J). An in-depth analysis

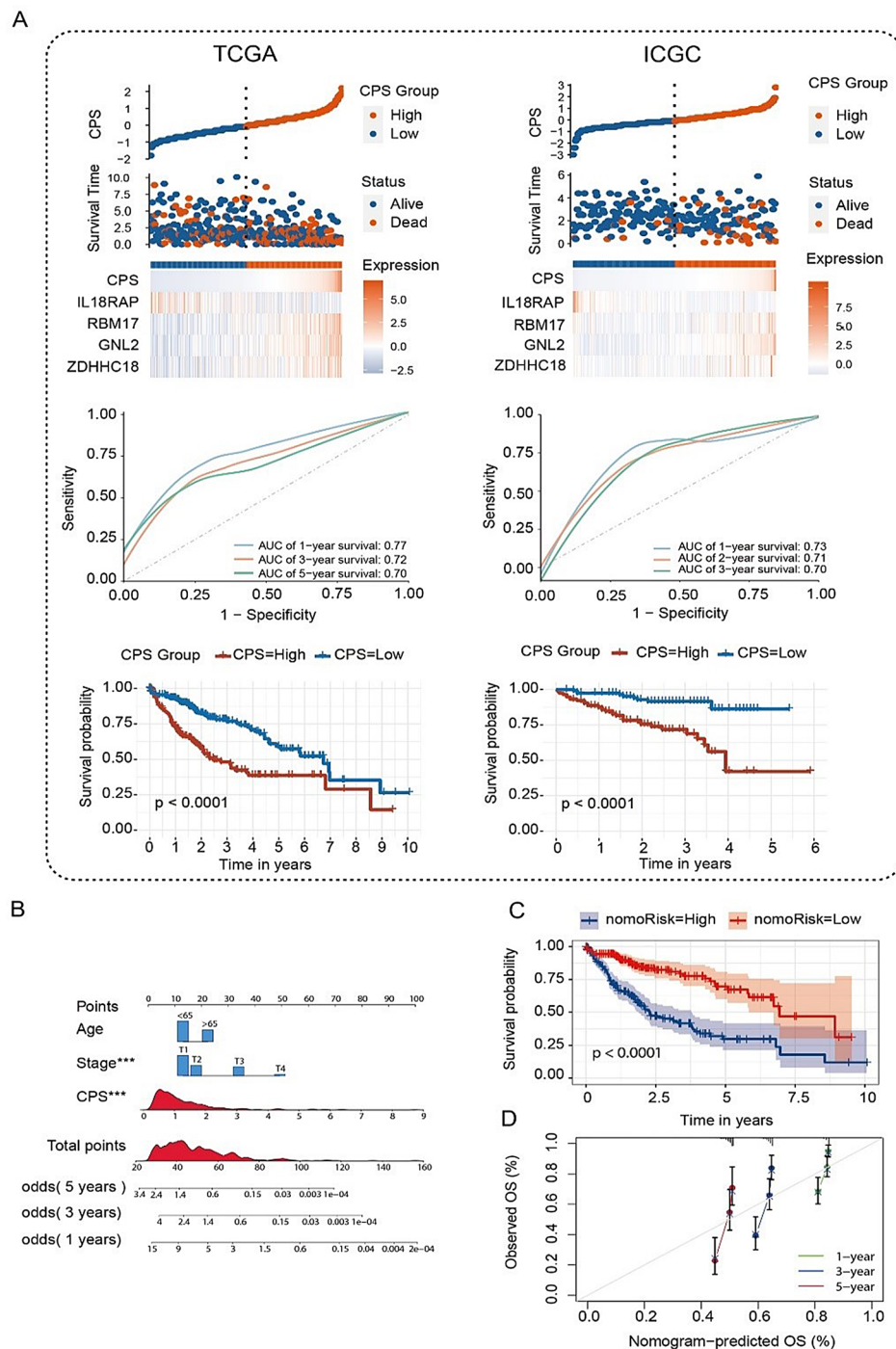


Fig. 8 Development of circadian prognosis scores to enhance liver cancer prognosis prediction. **(A)** Survival status, time distribution and model genes expression of patients in the high circadian prognosis scores (CPS) and low CPS groups (Top panels). Time-dependent receiver operating characteristic (ROC) curve analysis showing the area under curve values (AUC) for overall survival of TCGA and ICGC cohorts (Middle panels). Kaplan–Meier survival curves for liver cancer patients according to different risk types in TCGA and ICGC cohorts (Bottom panels). **(B)** The comprehensive nomogram for predicting probabilities of liver cancer patients with 1-, 3- and 5-year OS in the TCGA dataset. **(C)** Kaplan–Meier survival curves for liver cancer patients according to different nomoRisk types in TCGA cohort. **(D)** The calibration plots for predicting liver cancer patients with 1-, 3- and 5-year OS in the TCGA cohort. Nomogram-predicted probability of survival is plotted on the x-axis; actual survival is plotted on the y-axis. The Kaplan–Meier curves were analyzed using the log-rank test. CPS, Circadian prognostic scores; AUC, Area under the ROC Curve; OS, Overall survival; TCGA, The Cancer Genome Atlas; The Cancer Genome Atlas; ICGC, International Cancer Genome Consortium

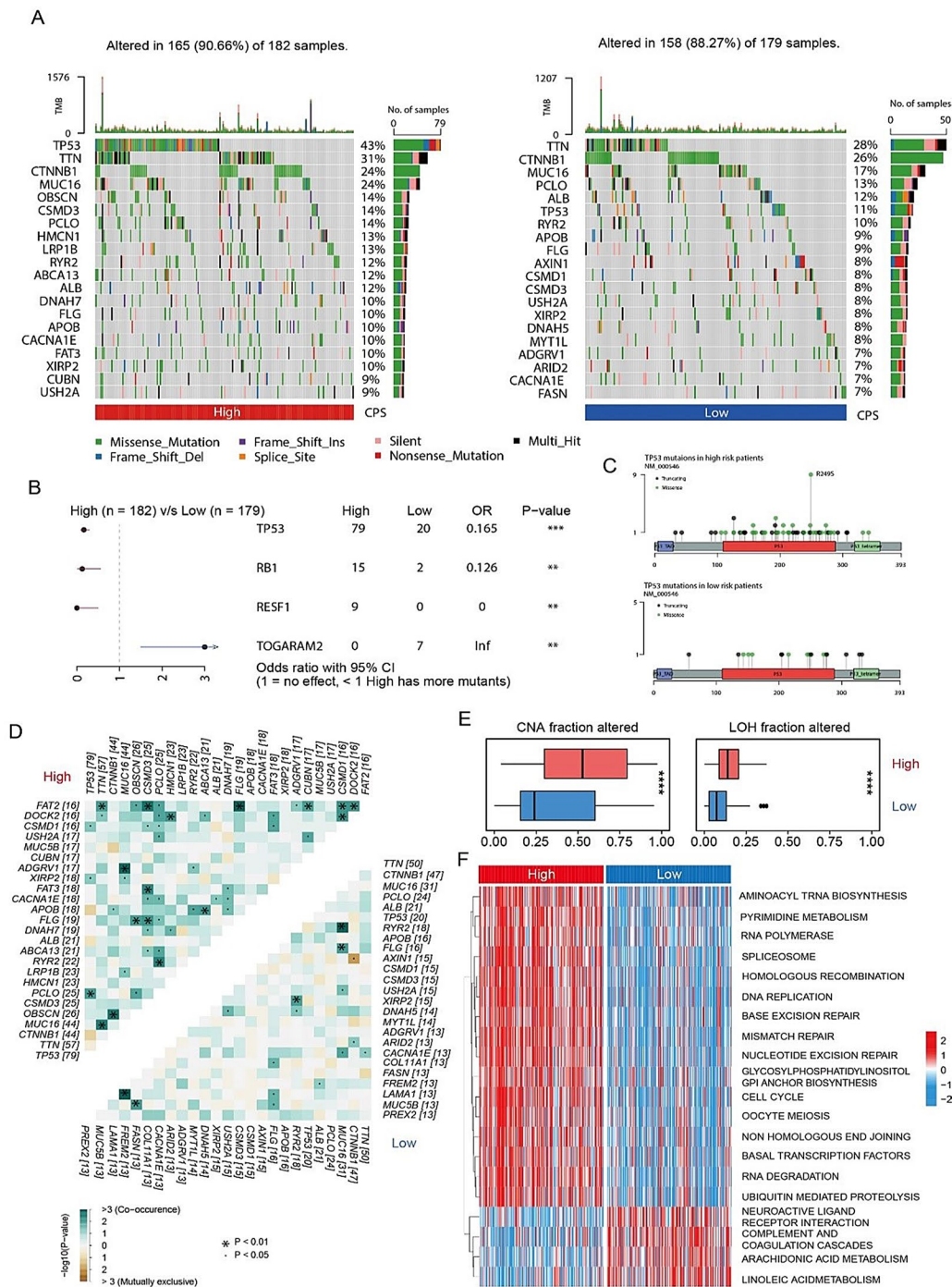


Fig. 9 Different genomic mutation landscapes and tumor-associated pathways among high- and low-risk groups. **(A)**. Mutations of top 20 genes in the TCGA-LICH cohort. Each column represents each sample, and each row represents each gene. Mutation type is marked by a distinct color. The left panel represents the high CPS groups and the right panel represents the low CPS groups. **(B)**. Forest plots of mutation bias in high CPS and low CPS groups. **(C)**. Lollipop plots of mutation sites in different CPS groups. **(D)**. Exclusive/co-occurrence mutation event heatmap. **(E)**. Copy number amplification (CNA) fraction and Loss of heterozygosity (LOH) fraction altered boxplot in different CPS groups. **(F)**. KEGG pathway enrichment heatmap in different CPS groups. * $P < 0.05$, ** $P < 0.01$, *** $P < 0.005$, **** $P < 0.001$, The P value was determined using the student t-test. CPS, circadian prognostic scores; TMB, tumor mutational burden; CNA, copy number amplification; LOH, loss of heterozygosity

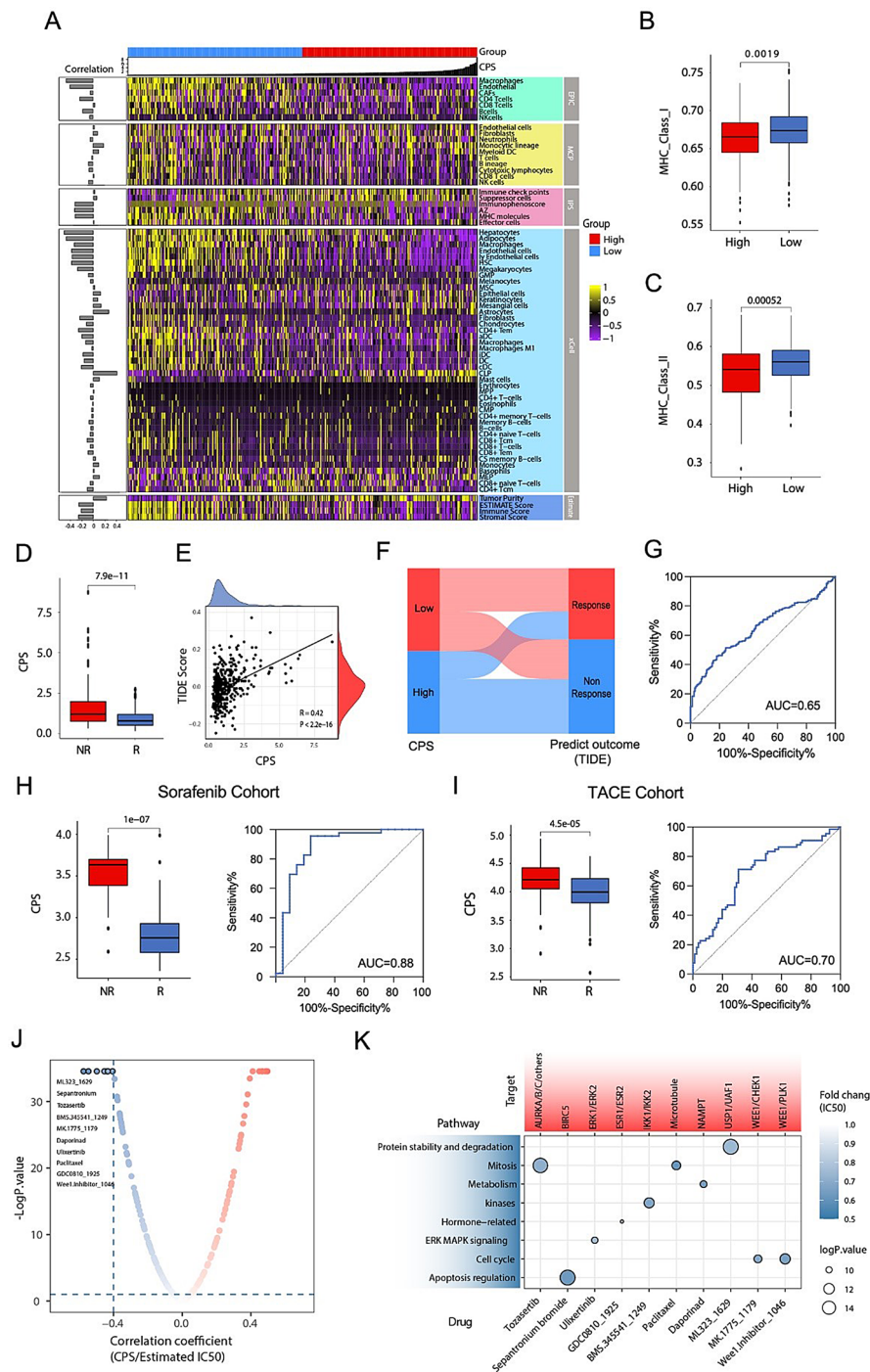


Fig. 10 Distinct immune microenvironments and responses to therapy among high- and low-risk groups. **(A)** Immune infiltration landscape of different CPS populations. The barplot on the left represents the correlation between CPS and immune cells. **(B)** Boxplot of MHC I scores calculated by GSVA method. **(C)** Boxplot of MHC II scores calculated by GSVA method. **(D)** Boxplot of CPS values in different ICB treatment response populations. **(E)** Scatterplot of correlation between Tide score and CPS. **(F)** Sankey diagram of CPS and immunotherapy response. **(G)** The Area Under Curve (AUC) of CPS reflects ICB response **(H)** Boxplot of CPS in different Sorafenib treatment response populations (left panel). The Area Under Curve (AUC) of CPS reflects the Sorafenib response (right panel). **(I)** Boxplot of CPS in different TACE treatment response populations (left panel). The Area Under Curve (AUC) of CPS reflects the TACE response (left panel). **(J)** Correlations rank plot of CPS and Estimated drugs IC50. Blue represents a negative correlation, while red represents a positive correlation. The dashed position represents the selected threshold. **(K)** MOA Dotplot for Screening Drugs Negatively Correlated with CPS. Pearson correlation analysis was performed to assess the correlations. Differences between the two groups were analyzed using a student t-test. CPS, Circadian prognostic scores; MHC, major histocompatibility complex; NR, non-response; R, response; AUC, Area under the ROC Curve; IC50, half-maximal inhibitory concentration

of the mechanism of action (MOA) of these identified compounds revealed a predominant targeting of cell cycle-related mechanisms, underscoring a putative vulnerability of high CPS patients to interventions targeting the cell cycle (Fig. 10K). Consistently, GSEA analysis revealed significant activation of cell cycle-related pathways in patients with high CPS (Supplementary Figure S3B).

Discussion

Our current study unveiled the multi-omics dysregulation of circadian rhythm in liver cancer, highlighting the intricate crosstalk between rhythm transcription factors, promoter methylation, copy number variations, and circadian dysregulation. Utilizing the ActivePathway approach, we constructed a multi-omics functional landscape of disordered circadian genes. The findings reveal extensive modulation of pathways implicated in cancer, EMT, cell proliferation, and immune-related pathways, as a consequence of circadian genes disruption. These insights underscore the pivotal role of circadian genes disturbance in the advancement of liver cancer.

Research employing humanized mouse models has elucidated that circadian disruption directly reprograms the transcriptome landscape of NASH and HCC, thereby accelerating the transition from HCC onset to the progression of HCC [7]. Despite these advances, pinpointing the specific critical circadian genes responsible for the advancement of liver cancer remains a considerable challenge.

In our study, RBM17, GNL2, ZDHHC18, and IL18RAP were identified as key dysregulated circadian genes through a machine learning approach. Furthermore, single-cell sequencing analysis revealed the dysregulation of these key circadian genes within the tumor microenvironment. Notably, our analysis highlighted the distinct expression of IL18RAP in cytotoxic CD8⁺ T cells, alongside its subsequent downregulation in the hepatic tumor milieu. This observation may elucidate the mechanism behind immune suppression induced by circadian dysregulation, offering insights into the intricate relationship between circadian gene expression and immune function within the tumor microenvironment. Another critical circadian signature gene, RBM17, known as a splicing-related RNA-binding protein, was further validated in our in-house HCC samples. RBM17 expression is markedly elevated in HCC relative to normal liver tissue and correlates with adverse prognostic outcomes. Our comprehensive multi-omics investigation, integrating, bulk, and single-cell transcriptomic datasets, indicates that the upregulation of RBM17 is associated with increased CNV scores, enhanced cell proliferation, EMT, poor differentiation, and augmented stemness characteristics. Experimental studies, both in vitro and in vivo, elucidate

that RBM17 significantly contributes to the proliferative and migratory properties of liver cancer cells. Furthermore, RBM17 is implicated in promoting CSC stemness and CD133 expression, alongside facilitating CSC-associated traits, especially in cisplatin resistance. Our study expands on the understanding of RBM17's role in mediating cisplatin resistance in HCC. Notably, CD133 has been well-established as a critical regulator of cisplatin resistance in cancers, with CD133⁺ cells demonstrating marked resistance to cisplatin treatment through mechanisms such as downregulation of PTEN and activation of the PI3K/AKT/mTOR signaling pathway [36, 37]. RBM17-mediated regulation of CD133 expression may therefore explain its involvement in modulating cisplatin sensitivity. The investigation into the role of RBM17 across various cancers, though limited, reveals a consistent pattern. Specifically, RBM17 is implicated in controlling cell proliferation in HCC, glioma, and hypopharyngeal carcinoma [38–40]. Moreover, it enhances CSC properties in colorectal cancer and acute myeloid leukemia, and influences the radiosensitivity and cisplatin sensitivity of lung and hypopharyngeal cancer cells, respectively [38, 41–43]. Additionally, disruptions in the circadian rhythm have been observed to significantly exacerbate cancer cell dissemination and lung metastasis in breast cancer, further enhancing tumor cell stemness and the tumor-initiating potential, while inducing an immune-suppressive metastatic tumor microenvironment [44]. Collectively, our findings furnish both bioinformatic and experimental substantiation linking RBM17 with liver tumorigenesis and elucidate a mechanistic connection between disrupted circadian rhythms and the enhanced stemness of cancer cells.

The Circadian Prognosis Scores (CPS) were developed to reflect circadian dysregulation in liver cancers. This approach may significantly optimize risk stratification, highlighting the role of liver circadian genes as robust prognostic classification factors. Furthermore, CPS is capable of precisely predicting the therapeutic responses of liver cancers to mainstream treatments such as sorafenib and TACE, in addition to immunotherapy. Moreover, CPS delineates distinct immune subtypes and pathway-enriched subtypes. Despite the resistance to TACE, sorafenib, and immunotherapy in cases presenting high CPS, analysis of the mechanism of action (MOA) reveals the therapeutic promise of drugs targeting the cell cycle for patients with elevated CPS. Supporting this, evidence derived from study on regenerating mouse livers suggests that the circadian clock regulates the expression of cell cycle-related genes, which in turn modulate the expression of the active cyclin B1-Cdc2 kinase, a key regulator of mitosis [45]. These findings underscore the vital interplay between circadian rhythm and cell cycle

modulation, suggesting a pronounced vulnerability of tumors with high CPS to cell cycle-targeted therapeutics.

The evolutionary history of liver cancer is rooted in its genome [46]. Among the genes, TP53 is the top mutated gene in HCC, with mutation frequencies ranging from 18 to 35.2% (average 25.9%) [47]. Intriguingly, our study indicates a notable bias towards high circadian disruption associated with TP53 mutations. This suggests an unexplored role of TP53 in circadian disruption in liver cancer. Supporting our findings, p53^{-/-} mice have a shorter period length that lacks stability, along with impaired photo-entrainment to a light pulses in a free-running condition [48]. Therefore, the intricate relationship between TP53 mutations and circadian disruption merits further investigation.

This study is subject to several limitations. First, the LCGs analyzed were identified through computational methods using the CYCLOPS algorithm, which infers rhythmicity without requiring time-of-day annotations. The adoption of this approach was necessitated by the formidable practical and ethical challenges associated with acquiring time-resolved human liver samples. Consequently, these LCGs are circadian-associated rather than rhythmically oscillating genes within the human sample datasets. Further experimental validation and phase-specific profiling are required. Secondly, although the prognostic significance of CPS was corroborated across multiple independent cohorts, our study lacks an internal cohort for validation purposes. Additionally, the evaluation of CPS's utility in immunotherapy was constrained by limited data, relying on the TIDE algorithm and a small cohort of HCC patients treated with PD-L1 inhibitors, which underscores the need for validation in a broader patient cohort. Lastly, despite suggesting that high CPS populations may benefit from cell cycle-targeted therapies, this hypothesis lacks validation through organoid models derived from patients.

In summary, our findings lay a foundational understanding of the interplay between liver circadian genes and liver cancer progression, paving a new avenue for identifying relevant therapeutic targets.

Conclusions

We constructed a CPS that is capable of predicting the prognosis and response to various treatments, including immune therapy. Furthermore, bioinformatics and functional evidence confirmed that RBM17, within the CPS, may play crucial regulatory roles in liver cancer. This positions RBM17 as a potential therapeutic target and prognostic biomarker for liver cancer.

Abbreviations

TF	Transcription factor
LCGs	Liver circadian genes
TME	Tumor microenvironment

CSC	Cancer stem cell
TCGA	The Cancer Genome Atlas
ICGC	International Cancer Genome Consortium
CNV	Copy number variation
cyCD8T	Cytotoxic CD8T cell
ex CD8T	Exhausted CD8T cell
Treg	Regulatory T cell
NK	Natural killer cells
B	B cell
Endo	Endothelial cell
CPS	Circadian prognostic scores
AUC	Area under the ROC Curve
OS	Overall survival
TMB	Tumor mutational burden
CAN	Copy number amplification
LOH	Loss of heterozygosity
MHC	Major histocompatibility complex
NR	Non-response
R	Response
IC50	Half-maximal inhibitory concentration

Supplementary Information

The online version contains supplementary material available at <https://doi.org/10.1186/s12935-025-03843-6>.

Supplementary Material 1

Supplementary Material 2

Supplementary Material 3

Supplementary Material 4

Acknowledgements

We'd like to thank Center for Computational Science and Engineering at Southern University of Science and Technology for computational support.

Author contributions

Jingsong Yan, Xiao Yang, Shaoyan Xi and Yan Li contributed to the study's conception and design. Data preparation, collection and analysis were performed by Jingsong Yan, Xiao Yang, Jiabin Lu, Shasha Wu, Yan Chen Wang, Yuyang Du, Jingyi Zheng, Fenfen Wang, Han Gao and Hui Yang. Jiabin Lu and Shaoyan Xi provided human samples and clinical data analyses. The draft of the manuscript was written by Jingsong Yan, Xiao Yang, Shaoyan Xi and Yan Li. All authors revised and approved the manuscript.

Funding

This work was supported by the National Natural Science Foundation of China (82372768 and 82073127), Guangdong Provincial Natural Science Fund (2022A1515012284), and Shenzhen Science and Technology Innovation Commission (JCYJ20220530115204011).

Data availability

All RNA-seq data used in this study are publicly available from the Gene Expression Omnibus (GEO, <http://www.ncbi.nlm.nih.gov/geo/>) database, The Cancer Genome Atlas (TCGA, <https://portal.gdc.cancer.gov/>), the China National Center for Bioinformation (CNCB, <https://ngdc.cnbc.ac.cn/>) and International Cancer Genome Consortium (ICGC, <https://dcc.icgc.org/>). The original experimental data and analysis code supporting the conclusions of this article are available from the corresponding author.

Declarations

Ethical approval

This study had been approved by the Committee for Ethical Review of Research Involving Human Subjects at the Sun Yat-Sen University Cancer Center and informed consent was obtained from the patients. Animal experiment approval was granted by the Institutional Animal Care and Use Committee at the Southern University of Science and Technology.

Consent for publication

All authors consent the publication of this work.

Competing interests

The authors declare no competing interests.

Received: 3 March 2025 / Accepted: 2 June 2025

Published online: 13 June 2025

References

- Llovet JM, Kelley RK, Villanueva A, Singal AG, Pikarsky E, Roayaie S, Lencioni R, Koike K, Zucman-Rossi J, Finn RS. Hepatocellular carcinoma. *Nat Rev Dis Primers*. 2021;7:6. <https://doi.org/10.1038/s41572-020-00240-3>.
- Pinyol R, Montal R, Bassaganyas L, Sia D, Takayama T, Chau GY, Mazzaferro V, Roayaie S, Lee HC, Kokudo N, Zhang Z, Torrecilla S, Moeini A, Rodriguez-Carunchio L, Gane E, Verslype C, Croitoru AE, Cillo U, de la Mata M, Lupo L, Strasser S, Park JW, Camps J, Solé M, Thung SN, Villanueva A, Pena C, Meinhardt G, Bruix J, Llovet JM. Molecular predictors of prevention of recurrence in HCC with Sorafenib as adjuvant treatment and prognostic factors in the phase 3 STORM trial. *Gut*. 2019;68:1065–75. <https://doi.org/10.1136/gutjnl-2018-316408>.
- Llovet JM, Zucman-Rossi J, Pikarsky E, Sangro B, Schwartz M, Sherman M, Gores G. Hepatocellular carcinoma. *Nat Rev Dis Primers*. 2016;2:16018. <https://doi.org/10.1038/nrdp.2016.18>.
- Bolshette N, Ibrahim H, Reinke H, Asher G. Circadian regulation of liver function: from molecular mechanisms to disease pathophysiology. *Nat Rev Gastroenterol Hepatol*. 2023;20:695–707. <https://doi.org/10.1038/s41575-023-00792-1>.
- Zhou D, Wang Y, Chen L, Jia L, Yuan J, Sun M, Zhang W, Wang P, Zuo J, Xu Z, Luan J. Evolving roles of circadian rhythms in liver homeostasis and pathology. *Oncotarget*. 2016;7:8625–39. <https://doi.org/10.18632/oncotarget.7065>.
- Saran AR, Dave S, Zarrinpar A. (2020). Circadian Rhythms in the Pathogenesis and Treatment of Fatty Liver Disease. *Gastroenterology*. 158, 1948–1966. <https://doi.org/10.1053/j.gastro.2020.01.050>
- Padilla J, Osman NM, Bissig-Choisat B, Grimm SL, Qin X, Major AM, Yang L, Lopez-Terrada D, Coarfa C, Li F, Bissig KD, Moore DD, Fu L. Circadian dysfunction induces NAFLD-related human liver cancer in a mouse model. *J Hepatol*. 2024;80:282–92. <https://doi.org/10.1016/j.jhep.2023.10.018>.
- Zhang Z, Liang Z, Gao W, Yu S, Hou Z, Li K, Zeng P. Identification of circadian clock genes as regulators of immune infiltration in hepatocellular carcinoma. *J Cancer*. 2022;13:3199–208. <https://doi.org/10.7150/jca.71925>.
- Ayan D, Cagatay A. Bioinformatic analysis of genetic changes CLOCK, BMAL1, CRY1, CRY2, PER1, PER2, PER3, and NPAS2 proteins in HCC patients. *Hepatol Forum*. 2023;4:108–17. <https://doi.org/10.14744/hf.2023.2023.0009>.
- Liang Y, Wang S, Huang X, Chai R, Tang Q, Yang R, Huang X, Wang X, Zheng K. (2021). Dysregulation of Circadian Clock Genes as Significant Clinic Factor in the Tumorigenesis of Hepatocellular Carcinoma. *Comput Math Methods Med*. 2021, 8238833. <https://doi.org/10.1155/2021/8238833>
- Qu M, Zhang G, Qu H, Yu A, Wu R, Tsukamoto H, Jia Z, Huang W, Lenz HJ, Rich JN, Kay SA. Circadian regulator BMAL1: CLOCK promotes cell proliferation in hepatocellular carcinoma by controlling apoptosis and cell cycle. *Proc Natl Acad Sci U S A*. 2023;120:e2214829120. <https://doi.org/10.1073/pnas.2214829120>.
- Zhang Z, Zeng P, Gao W, Zhou Q, Feng T, Tian X. Circadian clock: a regulator of the immunity in cancer. *Cell Commun Signal*. 2021;19:37. <https://doi.org/10.1186/s12964-021-00721-2>.
- Farshadi E, van der Horst GTJ, Chaves I. Molecular links between the circadian clock and the cell cycle. *J Mol Biol*. 2020;432:3515–24. <https://doi.org/10.1016/j.jmb.2020.04.003>.
- Wang Y, Narasimamurthy R, Qu M, Shi N, Guo H, Xue Y, Barker N. Circadian regulation of cancer stem cells and the tumor microenvironment during metastasis. *Nat Cancer*. 2024;5:546–56. <https://doi.org/10.1038/s43018-024-00759-4>.
- Lu Y, Yang A, Quan C, Pan Y, Zhang H, Li Y, Gao C, Lu H, Wang X, Cao P, Chen H, Lu S, Zhou G. A single-cell atlas of the multicellular ecosystem of primary and metastatic hepatocellular carcinoma. *Nat Commun*. 2022;13:4594. <https://doi.org/10.1038/s41467-022-32283-3>.
- Anafi RC, Francey LJ, Hogenesch JB, Kim J. CYCLOPS reveals human transcriptional rhythms in health and disease. *Proc Natl Acad Sci U S A*. 2017;114:5312–7. <https://doi.org/10.1073/pnas.1619320114>.
- Pizarro A, Hayer K, Lahens NF, Hogenesch JB. CircaDB: a database of mammalian circadian gene expression profiles. *Nucleic Acids Res*. 2013;41:D1009–1013. <https://doi.org/10.1093/nar/gks1161>.
- Liu CJ, Hu FF, Xie GY, Miao YR, Li XW, Zeng Y, Guo AY. GSCA: an integrated platform for gene set cancer analysis at genomic, Pharmacogenomic and Immunogenomic levels. *Brief Bioinform*. 2023;24. <https://doi.org/10.1093/bib/bbac558>.
- Paczkowska M, Barenboim J, Sintupisut N, Fox NS, Zhu H, Abd-Rabbo D, Mee MW, Boutros PC, Reimand J. Integrative pathway enrichment analysis of multivariate omics data. *Nat Commun*. 2020;11:735. <https://doi.org/10.1038/s41467-019-13983-9>.
- Kohl M, Wiese S, Warscheid B. Cytoscape: software for visualization and analysis of biological networks. *Methods Mol Biol*. 2011;696:291–303. https://doi.org/10.1007/978-1-60761-987-1_18.
- Hao Y, Stuart T, Kowalski MH, Choudhary S, Hoffman P, Hartman A, Srivastava A, Molla G, Madad S, Fernandez-Granda C, Satija R. Dictionary learning for integrative, multimodal and scalable single-cell analysis. *Nat Biotechnol*. 2024;42:293–304. <https://doi.org/10.1038/s41587-023-01767-y>.
- Gulati GS, Sikandar SS, Wesche DJ, Manjunath A, Bharadwaj A, Berger MJ, Ilagan F, Kuo AH, Hsieh RW, Cai S, Zabala M, Scheeren FA, Lobo NA, Qian D, Yu FB, Dirbas FM, Clarke MF, Newman AM. Single-cell transcriptional diversity is a hallmark of developmental potential. *Science*. 2020;367:405–11. <https://doi.org/10.1126/science.aax0249>.
- Trapnell C, Cacchiarelli D, Grimsby J, Pokharel P, Li S, Morse M, Lennon NJ, Livak KJ, Mikkelsen TS, Rinn JL. The dynamics and regulators of cell fate decisions are revealed by pseudotemporal ordering of single cells. *Nat Biotechnol*. 2014;32:381–6. <https://doi.org/10.1038/nbt.2859>.
- Fustero-Torre C, Jiménez-Santos MJ, García-Martín S, Carretero-Puche C, García-Jimeno L, Ivanchuk V, Di Domenico T, Gómez-López G, Al-Shahrour F. Beyondcell: targeting cancer therapeutic heterogeneity in single-cell RNA-seq data. *Genome Med*. 2021;13:187. <https://doi.org/10.1186/s13073-021-01001-x>.
- Wu R, Guo W, Qiu X, Wang S, Sui C, Lian Q, Wu J, Shan Y, Yang Z, Yang S, Wu T, Wang K, Zhu Y, Wang S, Liu C, Zhang Y, Zheng B, Li Z, Zhang Y, Shen S, Zhao Y, Wang W, Bao J, Hu J, Wu X, Jiang X, Wang H, Gu J, Chen L. Comprehensive analysis of Spatial architecture in primary liver cancer. *Sci Adv*. 2021;7:eabg3750. <https://doi.org/10.1126/sciadv.abg3750>.
- Friedman J, Hastie T, Tibshirani R. Regularization paths for generalized linear models via coordinate descent. *J Stat Softw*. 2010;33:1–22.
- Zeng D, Ye Z, Shen R, Yu G, Wu J, Xiong Y, Zhou R, Qiu W, Huang N, Sun L, Li X, Bin J, Liao Y, Shi M, Liao W. IOBR: Multi-Omics Immuno-Oncology biological research to Decode tumor microenvironment and signatures. *Front Immunol*. 2021;12:687975. <https://doi.org/10.3389/fimmu.2021.687975>.
- Wang Y, Hu P, Wang F, Xi S, Wu S, Sun L, Du Y, Zheng J, Yang H, Tang M, Gao H, Luo H, Lv Y, Yan J, Ou X, Li Y. UHRF1 Inhibition epigenetically reprograms cancer stem cells to suppress the tumorigenic phenotype of hepatocellular carcinoma. *Cell Death Dis*. 2023;14:381. <https://doi.org/10.1038/s41419-023-05895-w>.
- Ko CH, Takahashi JS. Molecular components of the mammalian circadian clock. *Hum Mol Genet* 15 Spec No. 2006;2:R271–277. <https://doi.org/10.1093/hmg/ddl207>.
- Vitaterna MH, King DP, Chang AM, Kornhauser JM, Lowrey PL, McDonald JD, Dove WF, Pinto LH, Turek FW, Takahashi JS. Mutagenesis and mapping of a mouse gene, clock, essential for circadian behavior. *Science*. 1994;264:719–25. <https://doi.org/10.1126/science.8171325>.
- Preitner N, Damiola F, Lopez-Molina L, Zakany J, Duboule D, Albrecht U, Schibler U. The orphan nuclear receptor REV-ERB α controls circadian transcription within the positive limb of the mammalian circadian oscillator. *Cell*. 2002;110:251–60. [https://doi.org/10.1016/s0092-8674\(02\)00825-5](https://doi.org/10.1016/s0092-8674(02)00825-5).
- Mohawk JA, Green CB, Takahashi JS. Central and peripheral circadian clocks in mammals. *Annu Rev Neurosci*. 2012;35:445–62. <https://doi.org/10.1146/annurev-neuro-060909-153128>.
- Lee Y, Tanggono AS. Potential role of the circadian clock in the regulation of Cancer stem cells and Cancer therapy. *Int J Mol Sci* 23. 2022. <https://doi.org/10.3390/ijms232214181>.
- Huang T, Song X, Xu D, Tiek D, Goenka A, Wu B, Sastry N, Hu B, Cheng SY. Stem cell programs in cancer initiation, progression, and therapy resistance. *Theranostics*. 2020;10:8721–43. <https://doi.org/10.7150/thno.41648>.
- Vogelstein B, Papadopoulos N, Velculescu VE, Zhou S, Diaz LA Jr, Kinzler KW. Cancer genome landscapes. *Science*. 2013;339:1546–58. <https://doi.org/10.1126/science.1235122>.

36. Liu F, Qian Y. The role of CD133 in hepatocellular carcinoma. *Cancer Biol Ther*. 2021;22:291–300. <https://doi.org/10.1080/15384047.2021.1916381>.
37. Lu R, Zhao G, Yang Y, Jiang Z, Cai J, Hu H. Inhibition of CD133 overcomes cisplatin resistance through inhibiting PI3K/AKT/mTOR signaling pathway and autophagy in CD133-Positive gastric Cancer cells. *Technol Cancer Res Treat*. 2019;18:1533033819864311. <https://doi.org/10.1177/1533033819864311>.
38. Wang X, Chen D, Han G, Wang X, Liu X, Xu B, Liu W, Li H, Zhang M, Ma S, Han Y. Downregulation of RBM17 enhances cisplatin sensitivity and inhibits cell invasion in human hypopharyngeal cancer cells. *Open Med (Wars)*. 2023;18:20230669. <https://doi.org/10.1515/med-2023-0669>.
39. Lu J, Li Q, Cai L, Zhu Z, Guan J, Wang C, Xia J, Xia L, Wen M, Zheng W, Su Z, Wang C. RBM17 controls apoptosis and proliferation to promote glioma progression. *Biochem Biophys Res Commun*. 2018;505:20–8. <https://doi.org/10.1016/j.bbrc.2018.09.056>.
40. Li C, Ge S, Zhou J, Peng J, Chen J, Dong S, Feng X, Su N, Zhang L, Zhong Y, Deng L, Tang X. Exploration of the effects of the CYCLOPS gene RBM17 in hepatocellular carcinoma. *PLoS ONE*. 2020;15:e0234062. <https://doi.org/10.1371/journal.pone.0234062>.
41. Liu L, Vujovic A, Deshpande NP, Sathe S, Anande G, Chen HTT, Xu J, Minden MD, Yeo GW, Unnikrishnan A, Hope KJ, Lu Y. The splicing factor RBM17 drives leukemic stem cell maintenance by evading nonsense-mediated decay of pro-leukemic factors. *Nat Commun*. 2022;13:3833. <https://doi.org/10.1038/s41467-022-31155-0>.
42. Qu H, Shi X, Xu Y, Qin H, Li J, Cai S, Zhao J, Wan B, Yang Y, Li B. (2024). Mechanism of Musashi2 affecting radiosensitivity of lung cancer by modulating DNA damage repair. *MedComm* (2020). 5, e548. <https://doi.org/10.1002/mco.2.548>
43. Fu Y, Bai C, Wang S, Chen D, Zhang P, Wei H, Rong F, Zhang C, Chen S, Wang Z. AKT1 phosphorylates RBM17 to promote Sox2 transcription by modulating alternative splicing of FOXM1 to enhance cancer stem cell properties in colorectal cancer cells. *Faseb J*. 2023;37:e22707. <https://doi.org/10.1096/fj.2021255R>.
44. Hadadi E, Taylor W, Li XM, Aslan Y, Villote M, Rivière J, Duvallet G, Auriou C, Dulong S, Raymond-Letron I, Provot S, Bennaceur-Grisicelli A, Acloque H. Chronic circadian disruption modulates breast cancer stemness and immune microenvironment to drive metastasis in mice. *Nat Commun*. 2020;11:3193. <https://doi.org/10.1038/s41467-020-16890-6>.
45. Matsuo T, Yamaguchi S, Mitsui S, Emi A, Shimoda F, Okamura H. Control mechanism of the circadian clock for timing of cell division in vivo. *Science*. 2003;302:255–9. <https://doi.org/10.1126/science.1086271>.
46. Zhuravleva E, O'Rourke CJ, Andersen JB. Mutational signatures and processes in hepatobiliary cancers. *Nat Rev Gastroenterol Hepatol*. 2022;19:367–82. <https://doi.org/10.1038/s41575-022-00587-w>.
47. Hussain SP, Schwank J, Staib F, Wang XW, Harris CC. TP53 mutations and hepatocellular carcinoma: insights into the etiology and pathogenesis of liver cancer. *Oncogene*. 2007;26:2166–76. <https://doi.org/10.1038/sj.onc.1210279>.
48. Miki T, Matsumoto T, Zhao Z, Lee CC. p53 regulates Period2 expression and the circadian clock. *Nat Commun*. 2013;4:2444. <https://doi.org/10.1038/ncomms3444>.

Publisher's note

Springer Nature remains neutral with regard to jurisdictional claims in published maps and institutional affiliations.